

A multi-resolution analysis of the radio-FIR correlation in the Large Magellanic Cloud

A. Hughes^{1,2*}, T. Wong^{2,3†}, R. Ekers², L. Staveley-Smith²,
 M. Filipovic^{2,4}, S. Maddison¹, Y. Fukui⁵, N. Mizuno⁵

¹ Centre for Supercomputing and Astrophysics, Swinburne University of Technology, Hawthorn VIC 3122, Australia

² CSIRO Australia Telescope National Facility, PO Box 76, Epping NSW 1710, Australia

³ Department of Astrophysics and Optics, School of Physics, University of New South Wales, Sydney NSW 2052, Australia

⁴ University of Western Sydney, Locked Bag 1797, Penrith South, DC, NSW 1797, Australia

⁵ Department of Astrophysics, Nagoya University, Chikusa-ku, Nagoya 464-8602, Japan

Accepted 2006 April 20. Received 2006 April 19; in original form 2006 January 27

ABSTRACT

We investigate the local correlation between the 1.4 GHz radio continuum and 60 μ m far-infrared (FIR) emission within the Large Magellanic Cloud (LMC) on spatial scales between 0.05 and 1.5 kpc. On scales below \sim 1 kpc, the radio-FIR correlation is clearly better than the correlation of the cold gas tracers with either the radio or the FIR emission. For the LMC as a whole, there is a tight correlation between the radio and FIR emission on spatial scales above \sim 50 pc. By decomposing the radio emission into thermal and non-thermal components, however, we show that the scale on which the radio-FIR correlation breaks down is inversely proportional to the thermal fraction of the radio emission: regions that show a strong correlation to very small scales are the same regions where the thermal fraction of the radio emission is high. Contrary to previous studies of the local radio-FIR correlation in the LMC, we show that the slope of the relation between the radio and FIR emission is non-linear. In bright star-forming regions, the radio emission increases faster than linearly with respect to the FIR emission (power-law slope of \sim 1.2), whereas a flatter slope of \sim 0.6 – 0.9 applies more generally across the LMC. Our results are consistent with a scenario in which the UV photons and cosmic rays in the LMC have a common origin in massive star formation, but the cosmic rays are able to diffuse away from their production sites. Our results do not provide direct evidence for coupling between the magnetic field and the local gas density, but we note that synchrotron emission may not be a good tracer of the magnetic field if cosmic rays can readily escape the LMC.

Key words: galaxies: individual (Large Magellanic Cloud) – ISM: galaxies – radio continuum: galaxies – infrared: galaxies – Magellanic Clouds

1 INTRODUCTION

The tight, almost ubiquitous correlation between the far-infrared (FIR) and radio continuum emission in star-forming galaxies remains one of the most robust, yet puzzling, relationships in extragalactic astronomy (see e.g. Yun et al. 2001, see also Fig. 1). The correlation is essentially linear over five orders of magnitudes in luminosity with a dispersion of less than 50%. It applies to galaxies beyond $z = 1$ (Appleton et al. 2004) and encompasses a diverse range of galaxy types, including normal barred and

unbarred spirals, dwarf and irregular galaxies, starbursts, Seyferts and radio-quiet quasars (for a review, see Condon 1992).

The conventional explanation for the radio-FIR correlation invokes massive star formation. In this model, the FIR emission is mostly thermal emission from dust that has been heated by the ultra-violet (UV) radiation from young massive stars. These same stars power the thermal radio emission of star-forming regions, and rapidly evolve to the supernovae whose remnants are responsible for accelerating the cosmic-ray electrons that produce the non-thermal component of the radio emission. The radio emission of normal spiral galaxies at centimetre wavelengths

* Email: ahughes@astro.swin.edu.au

† ARC-CSIRO Postdoctoral Linkage Fellow

2 *Hughes et al.*

is predominantly non-thermal (Condon 1992), while the total FIR emission comprises both a warm dust component, heated in H II regions by massive ($>20 M_{\odot}$) ionising stars, and a significant cool dust component that is heated by the interstellar radiation field (e.g. Walterbos & Schwering 1987). Efforts to decompose the radio emission into thermal and non-thermal components, and the FIR emission into warm and cool dust components, indicate that the overall radio-FIR correlation is constituted by a strong correlation between the thermal radio and the warm dust emission, and a weaker correlation between the non-thermal radio and the cool dust emission (Hoernes et al. 1998).

Although a correlation between warm dust and thermal radio emission from ionised gas is hardly surprising, the mechanism by which the dust grains couple to synchrotron emission arising through the interactions of relativistic electrons with the ambient magnetic field remains highly uncertain. Helou & Bicay (1993) have suggested a coupling between magnetic field strength and gas density, which would ensure a tight radio-FIR correlation in spite of the sensitive dependence of the synchrotron emission on the magnetic field. Variations on this idea have been discussed by Hoernes et al. (1998) and Murgia et al. (2005), the latter also connecting the radio-FIR correlation to the observed CO-radio correlation, as CO traces the dense molecular gas. An important constraint on these models is the scale on which the correlation breaks down, as this would shed light on the physical mechanism of the coupling (e.g., static pressure equilibrium predicts that the correlation should hold on scales greater than the scale height of a galaxy's gas disc).

Observationally, FIR and radio maps of nearby spiral galaxies generally show good correspondence, although studies of nearby spirals are limited to scales above a few hundred parsecs (e.g. Hoernes et al. 1998; Hippelein et al. 2003). On much smaller scales, detailed maps of the gas within several kiloparsecs of the Sun indicate that the radio emission from star-forming regions is predominantly thermal, and does not follow the radio-FIR correlation for integrated galaxy luminosities (e.g. Boulanger & Perault 1988; Haslam & Osborne 1987). Galactic supernova remnants do not seem to be well-correlated with FIR or mid-infrared (MIR) emission, or with sites of star formation (Cohen & Green 2001; Whiteoak & Green 1996). A tight, linear correlation between the integrated radio and FIR emission in galaxies is thus not at all expected from observations of the local interstellar medium (ISM). In light of this conflict, and the different effective scales of proposed mechanisms for the origin of the radio-FIR correlation, it seems timely to study the radio and FIR emission of a galaxy on intermediate spatial scales between those accessible in the Milky Way and in nearby spirals.

The aim of this study is to investigate the radio-FIR correlation within the Large Magellanic Cloud (LMC). The LMC is a gas-rich dwarf galaxy that exhibits clear signs of active star formation. Our global view of the LMC is complemented by sufficient spatial resolution to study the ISM structure in detail over a wide range of wavebands. At an assumed distance of 50.1 kpc (Alves 2004), 1 arcmin corresponds to 14.5 pc. The proximity of

the LMC thus allows a detailed comparison of the radio and FIR emission on scales down to 20 pc (for the highest resolution radio and FIR datasets that are currently available).

In addition to standard pixel-by-pixel techniques, we use a wavelet cross-correlation method for our analysis that allows us to quantify the correlation between different gas and dust tracers on spatial scales between ~ 0.04 and 2.0 kpc. To date, wavelets have enjoyed a limited (though rapidly increasing) application within astrophysics, but their ability to isolate signal simultaneously in the Fourier and spatial domains makes them ideal for analysing scale-dependent correlations in astronomical images.

The structure of this paper is as follows. In Section 2 we describe our data sets and reduction procedures. Our analysis methods and results are presented in Section 3. We discuss our results in the context of current models for the origin of the radio-FIR correlation in Section 4. Our conclusions are presented in Section 5.

2 OBSERVATIONAL DATA

The images we have used for this study are described in detail below, and summarized in Table 1. Originating from a variety of instruments, they cover different fields of view at different angular resolutions and pixel sizes. In order to compare the data, all maps were regridded to a common pixel size of 20 arcsec and a common J2000 map centre of $\alpha=5^{\text{h}}20^{\text{m}}38\overset{\text{s}}{.}6$, $\delta=-68^{\circ}41'22''$. Images of 1350^2 pixels, covering a roughly 7.5×7.5 region, were produced using an NCP projection, which is essentially an orthographic (SIN) projection with a tangent point at the north celestial pole. The final regridded, truncated images are shown in Fig. 2. Note that the region thus defined, which we refer to as the "whole LMC," is completely covered by all maps except for the CO map, which has a somewhat irregular sky coverage (Fig. 2). Total fluxes and flux densities measured within the selected region are given in Table 1.

Since we are interested in spatial variation of the radio-FIR correlation across the LMC, the maps were divided into 16 sub-regions, as shown in Fig. 2. Each sub-region is $1^{\circ}35 \times 1^{\circ}35$ in size, with 256×256 pixels and a pixel scale of 19 arcsec. The centre positions of the 16 sub-region maps are listed in Table 2, along with brief notes about the individual fields. Note the wide variation in flux density among sub-regions in the 1.4 GHz and $60 \mu\text{m}$ maps: for instance, sub-region 8, which covers the 30 Doradus region, contains roughly a third of the total radio and FIR emission in the LMC.

2.1 Far-Infrared Data

Infrared Astronomical Satellite (IRAS) mosaics of the LMC in the $60 \mu\text{m}$ and $100 \mu\text{m}$ bands were kindly provided to us by M. Braun and have been discussed by Braun et al. (1998). These data had been processed using the HIRAS algorithm, which uses the Pyramid Maximum Entropy (PME) method to improve upon the nominal resolution

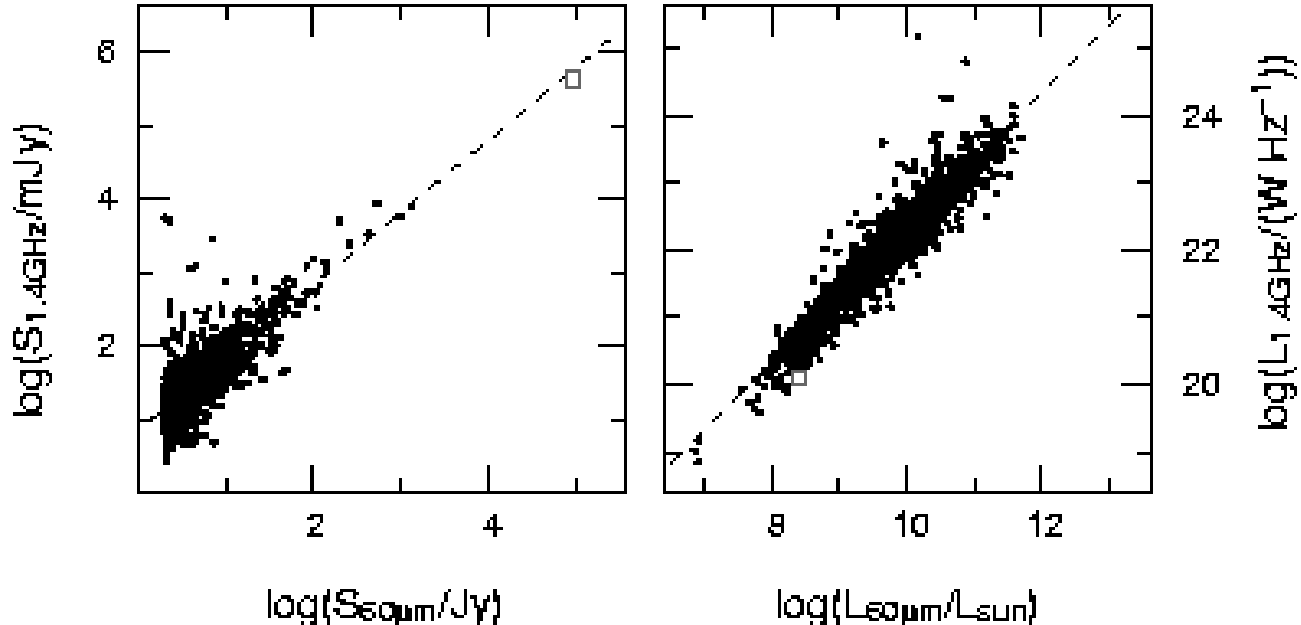


Figure 1. Plot of 1.4 GHz vs IRAS 60 μm flux density (*left*), and 1.4 GHz radio luminosity vs. IRAS 60 μm luminosity (*right*) for the Yun et al. (2001) sample of 1809 galaxies. In both panels, the dashed line is a linear least squares fit to the data. The LMC is indicated as an open square.

Table 1. Properties of the datasets used in this study, prior to any convolution or regridding. The fluxes and flux densities are measured over a roughly 7.5×7.5 region covering the main body of the LMC.

Band	Telescope(s)	Resolution (arcmin)	Pixel scale (arcmin)	Flux Density (Jy)
60 μm	IRAS (HIRAS)	1.3	0.25	9.64×10^4
60 μm	IRAS (IRIS)	4.0	1.5	9.61×10^4
100 μm	IRAS (HIRAS)	3.0	0.25	2.09×10^5
100 μm	IRAS (IRIS)	4.3	1.5	2.04×10^5
6.3 cm	Parkes	4.8	1.8	2.96×10^2
21 cm	Parkes	15.2	5.0	4.71×10^2
21 cm	ATCA+Parkes	0.67	0.22	4.26×10^2
Band	Telescope(s)	Resolution (arcmin)	Pixel scale (arcmin)	Flux (Jy km s $^{-1}$)
H I	ATCA+Parkes	1.0	0.33	3.98×10^5
CO	NANTEN	2.6	2.0	8.80×10^5

of the original IRAS survey data (4.0 ± 0.2 arcmin for the 60 μm band, and 4.3 ± 0.2 for the 100 μm band) (Bontekoe et al. 1994). The PME algorithm relies on the local sampling pattern in the IRAS survey, so the final resolution of HIRAS images varies spatially across a map. By fitting Gaussian profiles to point-like sources, we found that the resolution of the HIRAS maps was ~ 1.3 arcmin for the 60 μm data and ~ 3.0 arcmin for the 100 μm data. Measuring the average brightness for regions of sky away from the LMC, we determined a background level of 1.25 MJy sr $^{-1}$ for the 60 μm map and 3.0 MJy sr $^{-1}$ for the 100 μm map. These constant values were subtracted from the maps. A complete description of IRAS data products

can be found on the IRAS Documentation website.¹

To verify the flux density calibration of the HIRAS data, IRIS 60 μm and 100 μm maps were obtained from Dr. Miville-Deschénes at CITA (Miville-Deschénes & Lagache 2005). The IRIS images are at the same resolution as the original IRAS survey data, but have better zodiacal light subtraction and destriping than the equivalent IRAS Sky Survey images. The flux density calibration of IRIS is consistent with DIRBE data, but we found it was necessary to apply a small zero-level correction to the maps. Measuring the average brightness for regions of sky away from the LMC, we determined a background level of 0.85 MJy sr $^{-1}$ for the 60 μm map and 3.0 MJy sr $^{-1}$ for the 100 μm map. We subtracted these constant values from the maps. It is worth noting that the background levels measured for the IRIS maps are very similar to the background levels measured for the HIRAS maps, which increases our confidence in the flux density calibration of the HIRAS maps. A complete description of IRIS data products can be found on the IRIS website.²

2.2 Radio Continuum Data

We used a map of the 1.4 GHz radio continuum emission from the LMC produced by combining data from the ATNF Parkes 64 m telescope and the 6-element Australia Telescope Compact Array (ATCA).³ Details of the observations and data reduction were presented in papers by Kim et al.

¹ <http://irsa.ipac.caltech.edu/IRASdocs/toc.html>

² <http://www.cita.utoronto.ca/~mamd/IRIS/IrisOverview.html>

³ The Australia Telescope is funded by the Commonwealth of Australia for operation as a National Facility managed by CSIRO.

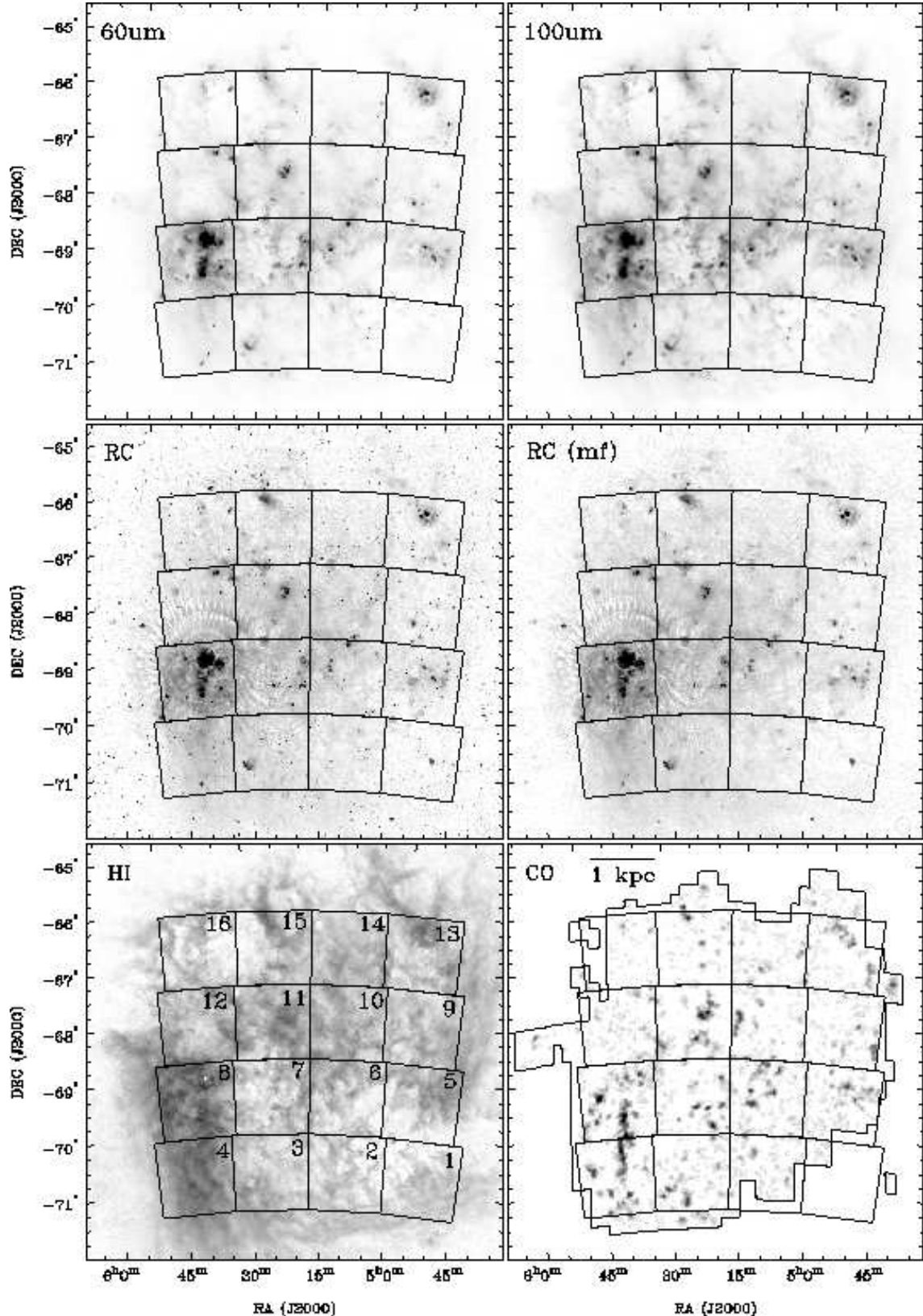


Figure 2. Maps of the Large Magellanic Cloud at different wavelengths, overlaid by the sub-region fields described in the text. The images correspond to HIRAS $60\text{ }\mu\text{m}$ emission (top left), HIRAS $100\text{ }\mu\text{m}$ emission (top right), ATCA+Parkes 1.4 GHz radio continuum (middle left), median filtered ATCA+Parkes 1.4 GHz radio continuum (middle right), ATCA+Parkes H I integrated intensity (bottom left), and NANTEN CO $J=1-0$ integrated intensity (bottom right). A square-root intensity scale has been used in displaying all images.

Table 2. Position centres, absolute and relative fluxes, and absolute and relative flux densities of the 16 sub-regions. Flux densities for the Parkes 1.4 and 4.8 GHz images are presented in Jy. The IRIS 60 μ m and 100 μ m flux densities are presented in 10^3 Jy. The fluxes for the H I and CO are presented in 10^4 Jy km s $^{-1}$. The relative contribution for a sub-region (shown in parentheses) is given as a percentage of the total emission in the entire region shown in Fig. 2.

Reg.	R. A. (J2000)	Dec. (J2000)	$S_{1.4}$ Jy	$S_{4.8}$ Jy	$S_{60\mu m}$ 10^3 Jy	$S_{100\mu m}$ 10^3 Jy	I_{HI} 10^4 Jy km s $^{-1}$	I_{CO} 10^4 Jy km s $^{-1}$	Notes
1	4:52:56	-70:49:30	4.4 (1%)	1.4 (0%)	0.6 (1%)	2.7 (1%)	0.9 (2%)	0.6 (1%)	
2	5:09:22	-70:49:30	9.0 (2%)	4.1 (1%)	1.4 (1%)	4.2 (2%)	0.9 (2%)	3.4 (4%)	
3	5:25:49	-70:49:30	20.7 (4%)	12.3 (4%)	2.7 (3%)	6.8 (3%)	1.5 (4%)	6.6 (7%)	
4	5:42:15	-70:49:30	25.4 (5%)	13.7 (5%)	2.9 (3%)	10.1 (5%)	4.1 (10%)	12.1 (14%)	
5	4:54:29	-69:28:30	14.0 (3%)	9.2 (3%)	3.8 (4%)	9.1 (4%)	1.5 (4%)	5.0 (6%)	
6	5:09:53	-69:28:30	21.8 (5%)	13.3 (5%)	6.0 (6%)	12.2 (6%)	1.5 (4%)	8.1 (9%)	
7	5:25:18	-69:28:30	39.4 (8%)	27.0 (9%)	8.1 (8%)	16.0 (8%)	1.6 (4%)	6.3 (7%)	N132D
8	5:40:42	-69:28:30	129.6 (28%)	107.2 (36%)	36.9 (38%)	53.5 (26%)	4.9 (12%)	16.5 (19%)	30 Dor
9	4:55:51	-68:07:30	8.3 (2%)	4.7 (2%)	2.0 (2%)	5.4 (3%)	1.6 (4%)	3.9 (4%)	
10	5:10:21	-68:07:30	21.0 (4%)	11.5 (4%)	3.5 (4%)	8.5 (4%)	2.1 (5%)	4.7 (5%)	
11	5:24:50	-68:07:30	34.2 (7%)	24.0 (8%)	7.6 (8%)	15.9 (8%)	2.6 (7%)	8.9 (10%)	
12	5:39:20	-68:07:30	24.7 (5%)	19.0 (6%)	4.8 (5%)	11.2 (5%)	2.3 (6%)	3.5 (4%)	
13	4:57:03	-66:46:29	14.1 (3%)	9.8 (3%)	3.7 (4%)	8.2 (4%)	1.9 (5%)	5.3 (6%)	N11
14	5:10:45	-66:46:29	11.8 (3%)	4.8 (2%)	1.6 (2%)	4.6 (2%)	1.7 (4%)	2.3 (3%)	PKS 0515-674
15	5:24:26	-66:46:29	17.8 (4%)	10.6 (4%)	2.6 (3%)	6.6 (3%)	1.5 (4%)	2.9 (3%)	
16	5:38:08	-66:46:29	13.1 (3%)	8.7 (3%)	1.9 (2%)	5.0 (2%)	1.0 (3%)	0.7 (1%)	

(1998, 2003). The angular resolution of the image is 40 arcsec, corresponding to a spatial resolution of 10 pc. The image suffers from ring-like artefacts at the $\sim 0.5\%$ level, presumably due to errors in the primary beam model used during the mosaicking and deconvolution process. These errors become significant close to bright compact sources such as the 30 Doradus region on the eastern side of the galaxy, limiting the sensitivity that can be achieved in these regions.

The 1.4 GHz image contains a large number of point sources, of which $\gtrsim 90\%$ are background AGN (Marx et al. 1997, Filipovic et al., in prep.). For the purpose of our study, it was desirable to remove these, since they lead to a spurious decorrelation on small scales. We found that most of the background radio sources could be eliminated by median filtering the image. The filtering operation, implemented in the GIPSY routine `mfilter`, moves a 2.5×2.5 window across a map, replacing the central pixel value (S_{cpix}) with the median value of the window (S_{med}) if $|S_{cpix} - S_{med}| > S_{med} + 1$ mJy. The 1 mJy offset prevents unnecessary filtering in noisy regions where the median is close to zero. The final median filtered radio continuum map is shown in Fig. 2 (*middle right*). For the whole LMC, the filter removed $\sim 10\%$ of the total emission in the 1.4 GHz map. For individual sub-regions, the fraction of the total emission removed by median filtering varies between a few percent, for sub-regions with strong emission from the LMC itself, to $\sim 40\%$ in sub-region 1. The ring artefacts surrounding extremely bright sources such as 30 Doradus (subregion 8), N132D (subregion 7) and PKS0515-674 (subregion 14) were not removed by median filtering.

Lower resolution radio maps of the LMC at 1.4 and 4.8 GHz were obtained from the Parkes surveys of Haynes et al. (1986, 1991) in order to estimate the large scale variation in the thermal fraction of the radio emission.

The angular resolutions of the single-dish 1.4 and 4.8 GHz radio maps are 15.2 and 4.8 arcmin respectively. Further details are presented in the paper by Filipovic et al. (1995).

2.3 H I Data

Kim et al. (2003) have combined Parkes single-dish neutral hydrogen observations of the LMC with an ATCA aperture synthesis mosaic to generate an H I data cube for the LMC with limiting angular resolution of 1 arcmin. The final dataset is sensitive to spatial scales above 15 pc across the heliocentric velocity range 190 km s $^{-1}$ to 388 km s $^{-1}$. The velocity resolution of the H I data is 1.65 km s $^{-1}$. An integrated intensity map was produced from the combined data cube by integrating over the heliocentric velocity range of 195 to 355 km s $^{-1}$ and clipping values with absolute value $< 2\sigma$. The use of clipping does bias the resulting map against low-level emission below the clipping value, but in total the excluded flux is only a small fraction ($\sim 8\%$) of the flux in an unclipped integrated map.

2.4 Molecular Gas Data

A survey in $^{12}\text{CO}(J=1-0)$ has been carried out by NAN-TEN, a 4m radio telescope operated by Nagoya University at Las Campanas Observatory in Chile. This new survey, introduced by Fukui et al. (2001), has achieved a sensitivity equivalent to $N(\text{H}_2) \sim 1.0 \times 10^{21} \text{ cm}^{-2}$, a factor of ~ 3 better than the original survey (Fukui et al. 1999; Mizuno et al. 2001). The data covers an irregularly shaped area of $\sim 6^\circ \times 6^\circ$ centered on the B1950 position ($5^\text{h}20^\text{m}00^\text{s}$, $-69^\circ00'00''$), and has revealed a distribution of 259 giant molecular clouds with 27,000 observed positions (Fukui et al. 2001). The half-power beam width of the telescope was 2.6 arcmin and data were taken with a 2 arcmin grid spacing. The spectrometers were two

acousto-optical spectrometers with 2048 channels each. The narrow-band (NB) spectrometer has a velocity coverage of 100 km s⁻¹ and a resolution of 0.1 km s⁻¹, whereas the wide-band (WB) spectrometer has a velocity coverage of 650 km s⁻¹ and a resolution of 0.65 km s⁻¹. Out of the 27,000 positions, 6229 were observed with the NB spectrometer, while the rest were observed with the newly developed WB spectrometer.

An integrated intensity map was produced from the NANTEN data cube as follows. The velocity channels were first binned to 1.95 km s⁻¹. To isolate regions of emission, a blanking mask was defined using the 3- σ contour of a smoothed version of the data cube; this cube had been generated by convolution of the binned cube with a Gaussian kernel with FWHM=5'.2. To create the integrated intensity map, the mask was applied to the original binned cube, which was then summed over local-standard-of-rest velocities of 200 to 300 km s⁻¹.

3 ANALYSIS

For this study, we are interested in both the structural correspondence between images taken in different wavebands and changes in the ratio of radio to FIR emission across the LMC. These considerations led us to adopt two techniques for our cross-correlation analysis: a wavelet method, which allows us to probe morphological correlations across the whole range of spatial scales present in each image, and a more traditional pixel-by-pixel comparison, which is sensitive to changes in the emission ratio as a function of position. We examine the FIR/radio ratio across the LMC in order to compare our results with other studies of the radio-FIR correlation in nearby disc galaxies.

Prior to conducting our analysis, maps of the whole LMC and the individual sub-regions were smoothed to a common resolution. For comparisons between the H I and 1.4 GHz continuum data, the continuum data were smoothed to 1 arcmin, i.e. the resolution of the H I data. For comparisons with the CO data, maps were smoothed to 3 arcmin, slightly larger than the FWHM of the NANTEN beam since the map was not Nyquist sampled. Comparisons involving the 60 μ m and 100 μ m maps were less straightforward, due to the spatially varying HIRAS resolution in response to survey coverage and signal-to-noise. We tested for potential resolution-dependent effects on our results by repeating our cross-correlation analysis with a HIRAS map smoothed to a range of resolutions between 1.5 and 5 arcmin. This simple validation test indicated that for most sub-regions the cross-correlation spectrum at small scales can be sensitive to changes in resolution, but only when the variation in the resolution is quite large (i.e. a factor of ~ 2). Visual inspection of the HIRAS data, however, suggested that the resolution of the map around 30 Doradus may be significantly lower than our nominal value of 1.3 arcmin. Further discussion of possible resolution effects on the cross-correlation results for this sub-region is presented in Section 3.4.

All the data preparation and analysis tasks in this study were performed with the MIRIAD, GIPSY and YORICK software packages (Sault et al. 1995; van der Hulst et al. 1992; Munro 1995).⁴

3.1 Pixel-by-pixel Analysis

The simplest measure of the correlation between two images, $f_1(x, y)$ and $f_2(x, y)$, with the same angular resolution and the same number of pixels is Pearson's linear correlation coefficient, r_p . This is a direct calculation of the correlation at each pixel:

$$r_p = \frac{\Sigma(f_{1i} - \langle f_1 \rangle)(f_{2i} - \langle f_2 \rangle)}{\sqrt{\Sigma(f_{1i} - \langle f_1 \rangle)^2} \sqrt{\Sigma(f_{2i} - \langle f_2 \rangle)^2}} \quad (1)$$

Identical images should have $r_p = 1$; images that are perfectly anti-correlated should have $r_p = -1$. The formal error on the correlation coefficient depends on the strength of the correlation and the number of independent pixels, n , in an image:

$$\Delta r_p = \frac{\sqrt{1 - r_p^2}}{\sqrt{n - 2}} \quad (2)$$

In our case, $n = 2601$ for the sub-region maps and $n = 72900$ for the whole LMC, so the formal error is small. The true error in the correlation coefficient is dominated by systematic errors in the data, such as calibration and zero-level uncertainties, which are not so easily quantified.

The correlation coefficients for the median filtered 1.4 GHz and 60 μ m emission in the whole LMC and individual sub-regions are presented in Table 3. The correlation between $\log S_{1.4}$ and $\log S_{60}$ was calculated, with flux densities expressed in Janskys. To ensure statistical independence, one in every five pixels along both axes were used for the calculation of r_p , corresponding to a separation of 1.7 arcmin for the whole LMC map, and 1.6 arcmin for the sub-region maps. For the whole LMC, $r_p=0.86$, while the median of the correlation coefficients for the sub-regions is 0.73. The correlation coefficients of individual sub-regions show a large scatter about this value, ranging between 0.36 and 0.91. As measured by Pearson's correlation coefficient, however, the correlation between the 1.4 GHz and 60 μ m (or 100 μ m) emission across the LMC is much stronger than the correlation found for other image pairs (see Table 4).

Given that a strong correlation is present, we can consider how the slope of the correlation varies between the individual sub-regions and the LMC as a whole. Scatter plots in logarithmic coordinates showing the flux density of the 60 μ m against the median filtered 1.4 GHz radio emission for the whole LMC and the individual sub-regions are shown in Figs. 3 and 4 respectively. As for Pearson's correlation coefficient, the plots are generated from maps that were smoothed to 1.5 arcmin resolution; the pixels that are used to construct the scatterplots are separated along both axes by 1.7 arcmin for the whole LMC maps, and 1.6 arcmin for the sub-regions. As many data points can occupy the same region in a plot, we indicate the distribution of

⁴ <http://yorick.sourceforge.net>

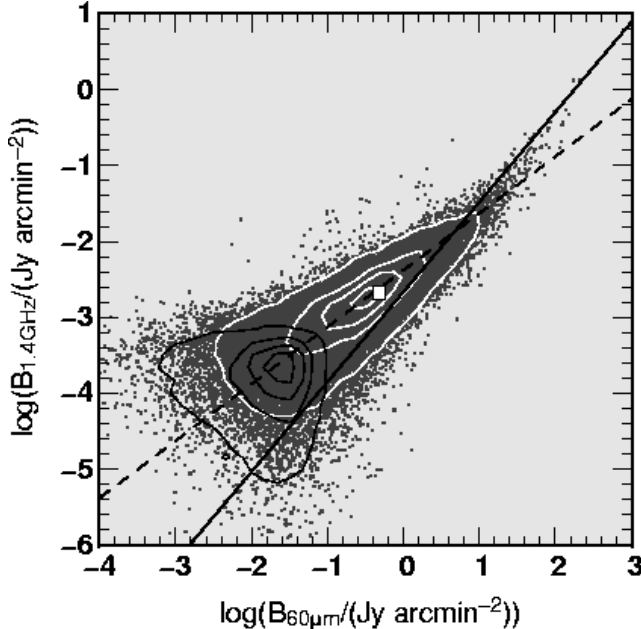


Figure 3. Pixel-by-pixel correlation between the 60 μm and median filtered 1.4 GHz maps of the LMC. The solid line is the WLS fit to the data (slope = 1.18), while the dashed line is the OLS fit (slope = 0.75). The white contours indicate the density of data points, with contour levels 5, 30, 60 and 90% of the distribution's peak density. The black contours, also with contour levels at 5, 30, 60 and 90% of the noise's peak density, indicate the distribution that would be expected for Gaussian noise with RMS appropriate to the 1.4 GHz and 60 μm images. The open square represents the average surface brightness for the whole LMC, calculated using the total ATCA+Parkes 1.4 GHz and IRIS 60 μm flux densities listed in Table 1, and a total galaxy area of $7^\circ.5 \times 7^\circ.5$.

the data points by binning the data into a 2-D histogram and showing contours of the 2-D distribution. The mesh used to define the contour levels consists of 60×60 cells, evenly distributed in logarithmic space between 10^{-7} and 10^3 Jy arcmin^{-2} for the FIR emission, and 10^{-9} and 10^1 Jy arcmin^{-2} for the radio emission.

For both the individual sub-regions and the whole LMC, we find that the local correlation between the radio and the 60 μm emission is reasonably good. We used two methods for calculating a linear fit to the pixel-by-pixel plots: weighted least squares (WLS) and the ordinary least squares (OLS) bisector. The WLS fit (solid line), implemented using the Numerical Recipes `fitexy` routine (Press et al. 1992), assumes an uncertainty of 2.3×10^{-4} Jy arcmin^{-2} for each 1.4 GHz measurement, and 2.7×10^{-2} Jy arcmin^{-2} for each 60 μm measurement. These uncertainties were estimated from the RMS of a blank region of sky in the 1.4 GHz and 60 μm LMC maps at 1.5 arcmin resolution. In logarithmic space, the high intensity pixels are thus given greater weighting due to their smaller relative errors (note that this assumes the errors are mainly additive rather than multiplicative). The OLS bisector (dashed line), implemented using the `slopes` routine provided by Feigelson & Babu (1992), assigns equal weight to each pixel and treats both variables symmetrically by determining the line which bisects the standard OLS solutions of Y on X and

X on Y. Measurement uncertainties are assumed to be unimportant compared to the intrinsic scatter in the data. We therefore expect that the WLS method will provide a better fit to the high-intensity pixels, whereas the OLS bisector will provide a better fit to the overall distribution of pixels. In order to prevent noise pixels contributing to our results, a 3σ cut was applied to the data prior to determining the fits.

For the whole LMC, the WLS method determined a slope of 1.18 to the data, while the OLS bisector indicated a flatter slope (0.75). Similar values are found for sub-regions 8 and 13, which contain the 30 Doradus and N11 star-forming complexes respectively. This is not surprising, since sub-region 8 is responsible for 38% (28%) of the LMC's total 60 μm (1.4 GHz) emission, and contributes significantly to the slope of WLS fit that we determine for the galaxy as a whole. The slopes of the WLS and OLS bisector fits in other sub-regions (listed in Table 3 and plotted in Fig. 4) show a range of values between 0.55 and 1.29. The median slope of the WLS fits is 0.78, while the median slope of the OLS bisectors is 0.75. Contrary to a previous study of the radio-FIR correlation in the LMC (Xu et al. 1992), our results suggest that locally there are two independent correlations between the radio and FIR emission, both of which are non-linear. The correlation in the bright star-forming regions is steeper than a linear correlation (slope \sim 1.1–1.3), and it is superimposed on a more general correlation that is flatter than a linear correlation (slope \sim 0.6–0.9). We compare our results to the Xu et al. (1992) result in Section 4.1, and discuss the variation of the WLS fit with the thermal fraction of the radio emission in Section 3.5.

Besides sub-regions 8 and 13, which contain 30 Dor and N11 and hence have a significant population of high-intensity pixels, the WLS fit and OLS bisector show greatest divergence in sub-region 1, where a large fraction of the emission is close to the sensitivity limit and the fit is therefore poorly constrained. The small congregation of points that show a high radio to FIR ratio in sub-region 1 is due to the bright supernova remnant 0450-70.9 (Mathewson et al. 1985).

Yun et al. (2001) derived a relation between the integrated 1.4 GHz and 60 μm emission from star-forming galaxies given by

$$\log(L_{1.4}/\text{W Hz}^{-1}) = (0.99 \pm 0.1) \log(L_{60}/L_\odot) + (12.07 \pm 0.08) .(3)$$

We used the data in their Table 1 to re-derive this relation in flux density units; a linear least squares fit gives

$$\log(S_{1.4}/\text{mJy}) = 0.98 \log(S_{60}/\text{Jy}) + 0.86 .(4)$$

These relations are shown as dashed lines in Fig. 1. On both panels, the LMC lies slightly below fits to the Yun et al. (2001) data. Furthermore, except for sub-regions 8 and 13, the slopes that we fit to the data points are flatter than a linear correlation. This causes the FIR/radio ratio to decrease for lower brightness regions, as has been noted in four nearby spiral galaxies by Murphy et al. (2005). Murphy et al. (2005) attribute this non-linearity of the local radio-FIR correlation to the diffusion of cosmic-ray electrons (CRe⁻s) away from star-forming sites, i.e. an

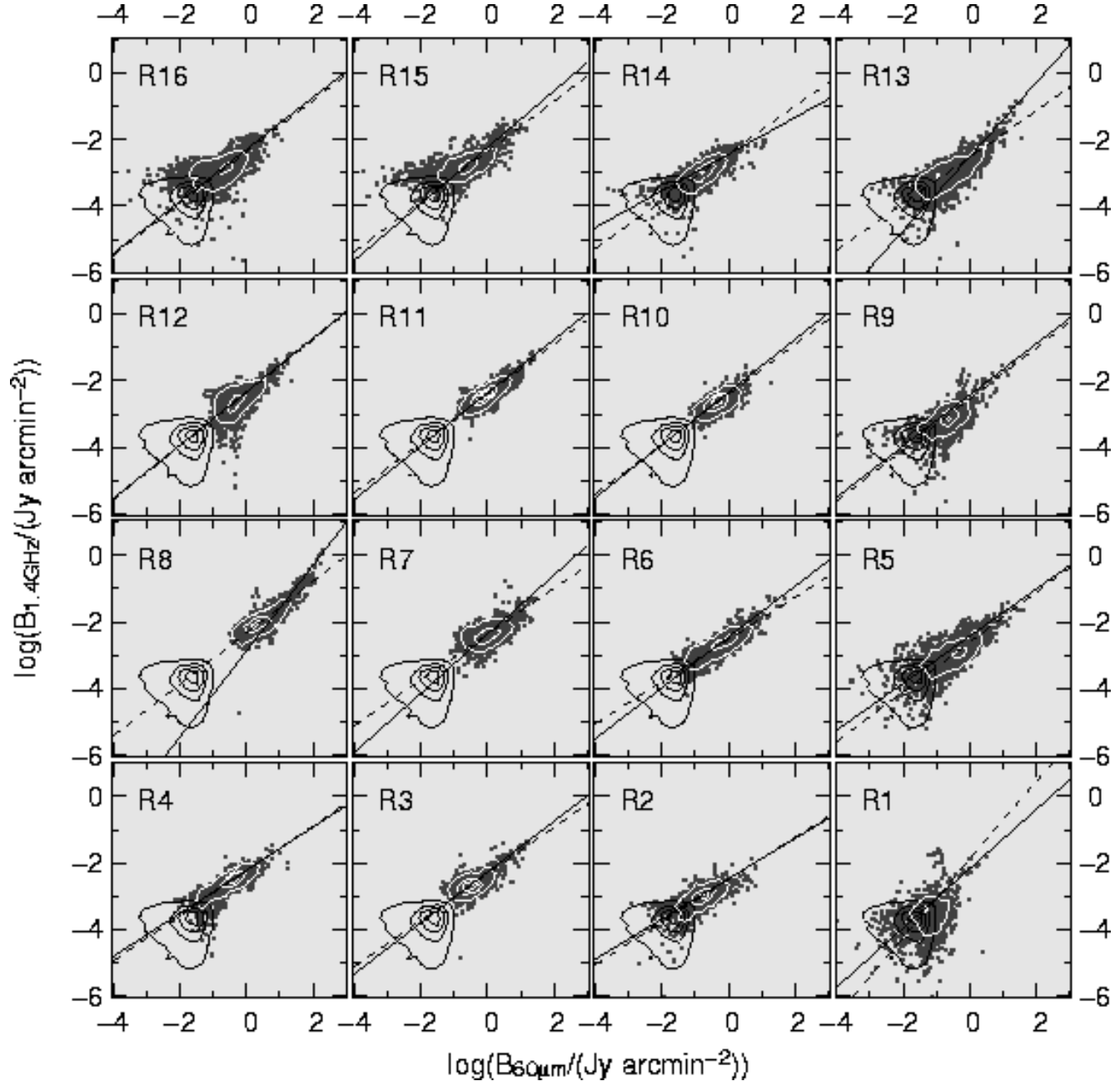


Figure 4. The pixel-by-pixel correlation between the $60\ \mu\text{m}$ and median filtered 1.4 GHz radio maps for individual sub-regions. The linear fits and noise contours (black) are the same as in Fig. 3. The white contours represent the density of the data points. The contour levels are 5, 30, 60 and 90% of the peak density in sub-region 11.

individual star-forming complex will show an infrared excess due to local dust heating by UV photons, but it also generates an extended non-thermal radio halo, whose radius depends on the mean age of the CRe⁻ population.

3.2 FIR/radio ratio map

In order to determine whether variations in the radio-FIR correlation correspond to particular physical structures in the LMC, we constructed a logarithmic FIR/radio ratio map (“ q -map”) from the IRIS 60 and $100\ \mu\text{m}$ maps, and the

ATCA+Parkes 1.4 GHz radio map. These input maps were each smoothed to a resolution of 4.3 arcmin, i.e. the natural resolution of the $100\ \mu\text{m}$ image. Following the convention of Helou et al. (1985), q is defined as

$$q = \log \left(\frac{\text{FIR}}{3.75 \times 10^{12} \text{ W m}^{-2}} \right) - \log \left(\frac{S_{1.4}}{\text{W m}^{-2} \text{ Hz}^{-1}} \right). \quad (5)$$

For each pixel, the total FIR surface brightness was determined from a combination of the IRIS 60 and $100\ \mu\text{m}$ maps according to Equation 6 of Yun et al. (2001),

$$\text{FIR} = 1.26 \times 10^{-14} (2.58 B_{60} + B_{100}) \text{ W m}^{-2}, \quad (6)$$

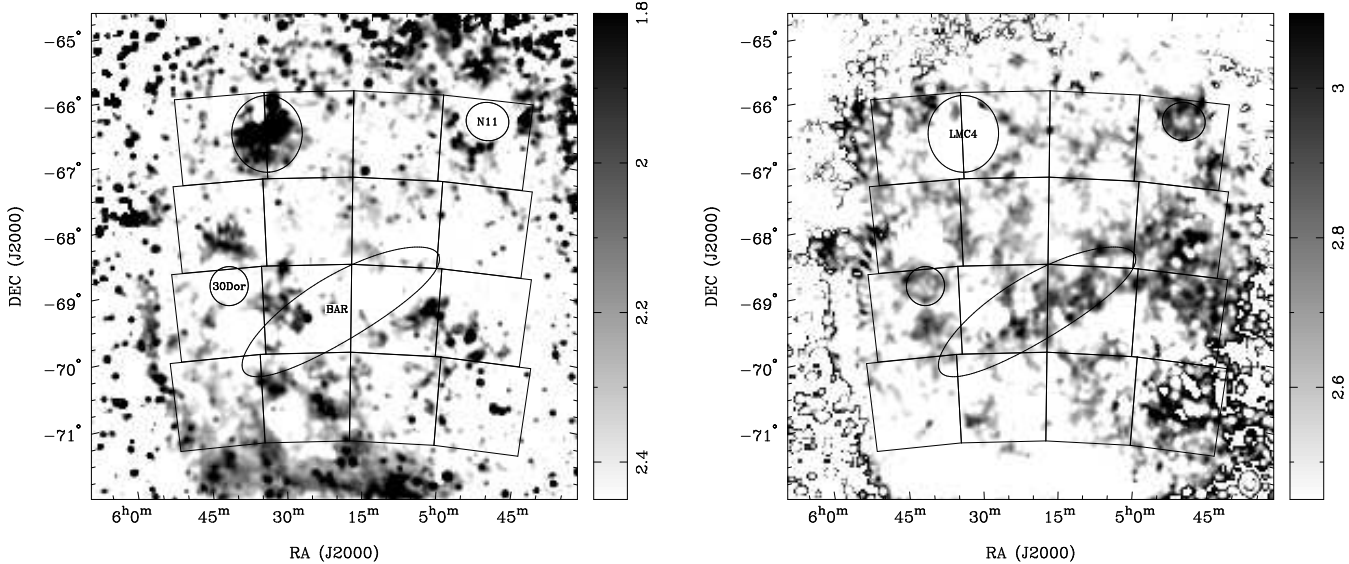


Figure 5. Images of the logarithmic FIR/radio ratio, q , constructed from the combined IRIS 60 and 100 μm maps and a smoothed version of the ATCA+Parkes 1.4 GHz radio map. The left panel shows regions where q is less than its median value of 2.45, whereas the right panel shows regions where $q > 2.45$. Major structural features of the LMC are indicated.

where B_{60} and B_{100} are the 60 and 100 μm surface brightness in Jy pix⁻¹ respectively.

The resultant map is shown in Fig. 5. For clarity, the left panel displays pixels for which $q > 2.45$, and the right panel displays pixels where $q < 2.45$. Only pixels detected above the 3σ level in the radio map were included in the calculation, which produces an irregular-shaped mask in the final map. The median q across the whole LMC is 2.45 ± 0.22 , where 0.22 is the semi-interquartile range. For the LMC as a whole, $q = 2.55$, calculated using the total flux density of the IRIS 60/100 μm and combined ATCA+Parkes 1.4 GHz maps. For comparison, the Yun et al. (2001) galaxy sample has a mean $q = 2.34$. Within the map boundaries where we calculate q , it thus appears that either the radio emission in the LMC is slightly underluminous compared to the value that we expect from the Yun et al. (2001) correlation, or that the FIR emission is slightly overluminous (see Fig. 3).

In contrast to some high-resolution q -maps of nearby disc galaxies (see e.g. Murphy et al. 2005), the most striking structures in the q -map of the LMC do not correspond to the brightest structures in the input FIR and radio maps (see Fig. 5). However, inspection of the q -map shows that the variation in the FIR/radio ratio across the LMC is spatially organized to some extent. In particular, the stellar bar region and the western edge of the LMC show elevated FIR/radio ratios, while the eastern side of the LMC shows numerous patches of low q values. The supershell LMC4 in the northeast is the largest of these low q regions (Meaburn 1980). Both 30 Doradus and N11 have a pronounced ring-like morphology in the q -map. The local peak in the original radio and FIR maps is surrounded by a ring of enhanced q values. An earlier low-resolution study by Klein et al. (1989) has reported that LMC H II regions have an average $q = 2.78$. Our data suggests that at higher angular resolution, the q value of an HII region can be separated into two distinct

components: a compact central region where the FIR and (mostly thermal) radio emission are high but q is quite close to the mean q across the whole LMC, and a ring of enhanced q values that arises through the different scale-lengths of the FIR and radio emission associated with the H II region. This morphology is consistent with the statistical detection of a “dip-and-ring” structure around LMC H II regions by Xu et al. (1992).

3.3 Wavelet Analysis

Wavelet analysis involves the convolution of an image with a family of self-similar basis functions that depend on scale and location. It can be useful to consider the wavelet transform as the general case of the Fourier transform, where the oscillatory functions are localised in both time and frequency. The family of basis functions is generated by dilating and translating a mother function, which is called the analysing wavelet. In this paper we make use of the two-dimensional continuous wavelet transform, which can be written as

$$W(a, \mathbf{x}) = w(a) \int_{-\infty}^{\infty} \int_{-\infty}^{\infty} f(\mathbf{x}') \psi^* \left(\frac{\mathbf{x}' - \mathbf{x}}{a} \right) d\mathbf{x}' \quad (7)$$

Here $f(\mathbf{x})$ is a two-dimensional function, such as an image, ψ^* is the complex conjugate of the dilated and translated analysing wavelet, and $w(a)$ is a normalising function. a is the scale size of the wavelet. Note that the term “continuous wavelet transform” is used in the literature to distinguish this transform from a “discrete” transform which employs an orthogonal set of basis functions; however, there is no fundamental difficulty applying the former to discretely sampled data such as astronomical images.

Our use of wavelet transforms follows closely the work of Frick et al. (2001), who pioneered their application to galaxy

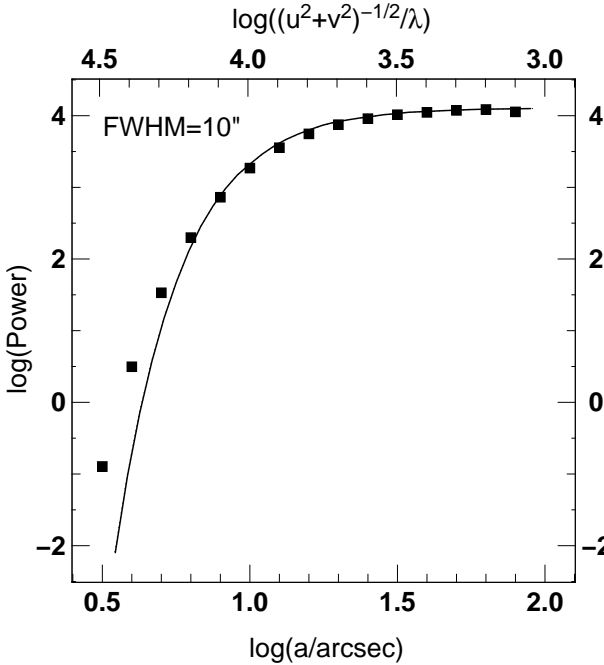


Figure 6. The wavelet (filled squares) and Fourier (solid line) power spectra for a $10''$ (FWHM) Gaussian.

images. Our analysing wavelet is their “Pet Hat” which can be written in Fourier space as

$$\hat{\psi}(ka) = \begin{cases} C(a) \cos^2\left(\frac{\pi}{2} \log_2 2|k|a\right) & : \frac{1}{4a} < |k| < \frac{1}{a} \\ 0 & : |k| < \frac{1}{4a}, |k| > \frac{1}{a} \end{cases} \quad (8)$$

This function picks out an annulus in the Fourier plane centred at $k=(2a)^{-1}$, and provides both simplicity and good separation of scales. The normalising factor $C(a)$ is chosen to provide unit total flux density in the wavelet image (or unit total flux, in the case of the H I and CO data). $C(a)$ is evaluated numerically to be $1.065a/\delta$, where a and δ are the scale size (defined below) and pixel size expressed in radians.

Throughout this paper we adopt the convention that an angular scale size a in radians corresponds to a spatial frequency of $(2a)^{-1}$ wavelengths. This is based on the observation that a positive, Gaussian-like structure will tend to couple with half of a sine wave rather than a full period, however it differs from the usual convention by a factor of 2. As an illustrative example, we show in Fig. 6 the wavelet and Fourier spectra for a $10''$ (FWHM) Gaussian; the spatial frequency is shown on the top axis and the corresponding spatial scales are shown on the bottom axis. In Table 3 and the following sections, we express a in arcseconds, which are a more appropriate unit for the size scales of interest here. The Fourier spectrum is defined in the usual way as $E_f(k) = |\hat{f}(k)|^2$.

Expressing the convolution of Equation 7 in terms of Fourier transforms, the *wavelet filtered image* is calculated as

$$W(a, \mathbf{x}) = \frac{1}{N^2} \sum_{(k_1, k_2)} \hat{f}(\mathbf{k}) \psi^*(\mathbf{k}a) e^{-2\pi i(\mathbf{k}\cdot\mathbf{x})/N}, \quad (9)$$

Table 3. Summary of the wavelet and pixel-by-pixel correlations between the median filtered 1.4 GHz and the $60 \mu\text{m}$ images for the whole LMC and individual sub-regions. Columns 2 and 3 list the angular (arcsec) and linear (parsec) spatial scales at which the wavelet cross-correlation falls below 0.75. Column 3 lists the Pearson’s correlation coefficient, r_p . Columns 4 and 5 list the WLS and OLS-bisector slopes. Column 6 lists the thermal fraction f_{th} of the radio emission at 1.4 GHz, assuming a non-thermal spectral index of -0.7 .

Region	$\log(a/\text{arcsec})$	Scale (pc)	r_p	slope _{WLS}	slope _{OLS}	f_{th}
LMC	2.3	50	0.86	1.18	0.75	0.45
1	3.0	>240	0.36	0.89	1.17	<0
2	2.7	120	0.57	0.60	0.64	0.07
3	2.4	60	0.79	0.76	0.70	0.37
4	3.0	>240	0.62	0.64	0.68	0.26
5	2.3	50	0.72	0.71	0.75	0.50
6	2.2	40	0.80	0.76	0.63	0.41
7	3.0	>240	0.48	0.89	0.69	0.57
8	2.2	40	0.89	1.29	0.77	0.87
9	2.2	40	0.77	0.77	0.77	0.33
10	2.8	150	0.58	0.79	0.75	0.27
11	2.1	30	0.91	0.80	0.74	0.60
12	1.9	20	0.86	0.80	0.80	0.75
13	2.1	30	0.85	1.11	0.70	0.58
14	2.9	150	0.55	0.55	0.71	<0
15	2.6	100	0.72	0.85	0.75	0.38
16	2.3	50	0.73	0.78	0.77	0.53

where N is the linear dimension of the image in pixels, and the *wavelet spectrum* as

$$E(a) = \sum_{(x_1, x_2)} |W(a, \mathbf{x})|^2. \quad (10)$$

This spectrum, which can be thought of as a smoothed version of the power spectrum, reveals the dominant energy scales in an image.

Finally we define the *wavelet cross-correlation coefficient* as

$$r_w(a) = \frac{\sum \sum W_1(a, \mathbf{x}) W_2(a, \mathbf{x})}{[E_1(a) E_2(a)]^{1/2}} \quad (11)$$

where the subscripts refer to two images of the same size. This is the wavelet analogue of the Fourier cross power spectrum. Following Frick et al. (2001), we assign an uncertainty of

$$\Delta r_w(a) = \frac{\sqrt{1 - r_w^2}}{\sqrt{n - 2}} \quad (12)$$

to this coefficient, where $n = (L/a)^2$ and L is the linear size of the image.

3.4 Wavelet Cross-correlations

The wavelet cross-correlation spectrum was calculated for each of the following map pairs: (a) radio and $60 \mu\text{m}$ emission; (b) radio and $100 \mu\text{m}$ emission; (c) radio and CO emission; (d) $60 \mu\text{m}$ and CO emission; (e) radio and H I emission; (f) $60 \mu\text{m}$ and H I emission; (g) $100 \mu\text{m}$ and H I emission; (h) CO and H I emission. The median

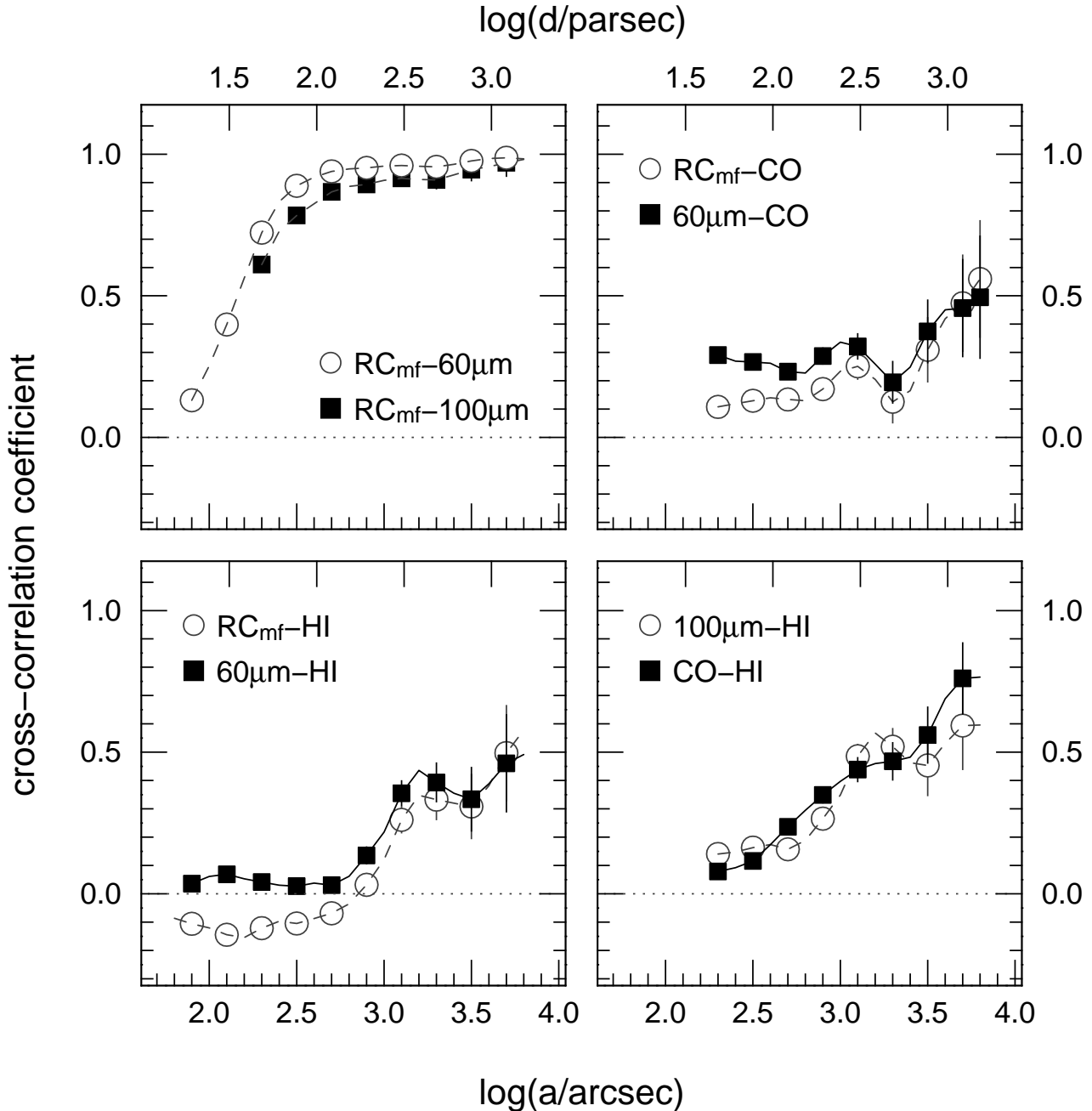


Figure 7. Wavelet cross-correlation spectra for emission from the whole LMC. *Top Left.* Median filtered 1.4 GHz radio vs. 60 μ m emission and median filtered 1.4 GHz radio vs. 100 μ m emission. *Top Right.* Median filtered 1.4 GHz radio vs. integrated CO emission and 60 μ m vs. CO emission. *Bottom Left.* Median filtered 1.4 GHz radio vs. integrated H I emission and 60 μ m vs. H I emission. *Bottom Right.* 100 μ m vs. H I emission and CO vs. H I emission. For all panels, the wavelet scale is indicated on the bottom axis, and the corresponding spatial scale (for an assumed LMC distance of 50.1 kpc) is shown on the top axis.

filtered 1.4 GHz map was used for the comparisons involving radio emission. We calculate the cross-correlation spectra on wavelet scales $\log(a) = 1.8 - 3.8$ for pair (e), $\log(a) = 1.9 - 3.8$ for pairs (a) and (f), and $\log(a) = 2.3 - 3.8$ for pairs (b), (c), (d), (g) and (h). For an LMC distance of 50.1 kpc, the range of spatial scales that we probe with all eight cross-correlation spectra is 0.05 – 1.5 kpc, extending down to 0.02 kpc for the highest resolution datasets. The

smallest scale that we can study is limited by the resolution of the data. The largest scale depends on the size of the field, and is determined such that the width of each map is equal to or greater than four times the largest wavelet scale. The results for all eight pairs are shown in Fig. 7 for the whole LMC. Figs. 8 and 9 show the results for pairs (a), (c), and (e) for the individual sub-regions, as well as the wavelet cross-correlation between the original (unfiltered) radio

image with the $60\text{ }\mu\text{m}$ emission. For the cross-correlation spectra of the sub-regions, the largest wavelet scale that we study is $\log(a) = 3.0$, corresponding to a spatial scale of $\sim 0.25\text{ kpc}$.

3.4.1 Cross-correlations between radio and FIR emission

For the whole LMC, it is clear that the correlation between the 1.4 GHz radio emission and the $60\text{ or }100\text{ }\mu\text{m}$ dust emission (Fig. 7, *top left*) is very strong, and significantly better at all spatial scales than the correlations that involve the molecular or atomic gas. Frick et al. (2001) regard values higher than 0.75 to be indicative of an excellent correlation between two images: by this measure, the correlation between the radio and $60\text{ }\mu\text{m}$ emission in the LMC remains strong down to spatial scales of $\sim 50\text{ pc}$ (210 arcsec). The correlation between the 1.4 GHz radio and the $100\text{ }\mu\text{m}$ dust emission is marginally worse across all scales, falling below 0.75 at $\sim 60\text{ pc}$ (250 arcsec). Nonetheless, it still appears that, averaged over the entire LMC, the radio-FIR correlation is maintained on scales less than the scale height of the gaseous disc, which has been estimated to be between 80–100 pc (Elmegreen et al. 2001) and 180 pc (Kim et al. 1999).

Since the emission of the LMC as a whole is strongly influenced by the 30 Dor region, we have also compared the median filtered 1.4 GHz and the $60\text{ }\mu\text{m}$ emission for individual sub-regions across the LMC (Fig. 8, *filled squares*). The spatial scale at which the correlation falls below 0.75 for each sub-region is listed in Table 3. Generally the correlation remains excellent, with half of the sub-regions showing a strong correlation down to spatial scales of $< 50\text{ pc}$ ($\log(a) \sim 2.3$). However, in several of the other sub-regions the correlation breaks down on much larger scales ($> 100\text{ pc}$, corresponding to $\log(a) \sim 2.6$). We demonstrate in Section 3.5 that there is an inverse relationship between the size scale of the correlation breakdown and the thermal fraction of the radio emission. Thus, the excellent correlation between the radio and $60\text{ }\mu\text{m}$ emission that we see in sub-regions such as 8 and 12 may be dominated by a correlation between the warm dust and the thermal radio emission, which does not drive the correlation between the total radio and FIR flux density of spiral galaxies.

Our results for the wavelet cross-correlations are fairly robust whether or not median filtering is used to suppress compact point sources. When the original (unfiltered) radio map is cross-correlated with the $60\text{ }\mu\text{m}$ map, the correlation generally degrades (Fig. 8, *open circles*), especially for fields at the edge of the LMC where the total emission is low and fewer of the compact point sources are presumably intrinsic (e.g. sub-regions 3, 9, and 14). However, the qualitative trends remain the same, since the compact sources usually dominate the emission only on the smallest wavelet scales. In a few cases (e.g. sub-regions 6 and 13) the median filtering appears to worsen the correlation, by removing emission from compact sources that have bright $60\text{ }\mu\text{m}$ counterparts and are thus likely to be H II regions.

On the other hand, an incorrect assumption about the

resolution of the input images (e.g., the HIRAS-processed IRAS images) could cause the correlation to break down on larger scales than it should. This is especially a concern in sub-region 8, which covers 30 Doradus. Wavelet power spectra for this sub-region show a steep decline below a scale of $\sim 250\text{ arcsec}$, whereas the power spectra for other sub-regions tend to steepen at smaller characteristic scales ($\sim 120\text{ arcsec}$), slightly larger than our estimate of the HIRAS resolution. Using an IRAS image processed with the HIRES deconvolution method (kindly provided to us by J. Surace at IPAC) results in a much stronger wavelet cross-correlation that exceeds 0.75 down to scales of 100 arcsec (Fig. 8, dashed line in R8). HIRES is an alternative re-processing of the IRAS survey, which, like HIRAS, aims to improve on the nominal resolution of the original IRAS survey data. HIRES uses the Maximum Correlation Method rather than the Pyramid Maximum Entropy algorithm used by HIRES, and achieves a resolution of $\sim 1\text{ arcmin}$ for the $60\mu\text{m}$ band. The discrepancy between the results of the wavelet cross-correlation for the HIRAS and HIRES data in sub-region 8 means that we cannot rule out the possibility that the radio-FIR correlation remains strong on even smaller scales than we deduce here, especially in the 30 Dor region, which constitutes a large fraction of the galaxy's emission. Future high-resolution data sets from *Spitzer* should be able to overcome these difficulties with the IRAS data.

3.4.2 Cross-correlations between other wavebands

Cross-correlations involving the CO and H I images for the whole LMC are shown in the last 3 panels of Fig. 7. For each image pair, the value of the wavelet cross-correlation at wavelet scales $\log(a) = 2.0, 2.5, 3.0$ and 3.5 (corresponding to spatial scales of 25, 80, 245 and 770 pc) is listed in Table 4. The relative weakness of these correlations compared to the radio-FIR correlations is immediately apparent. Indeed, the strength of the radio-FIR correlation is such that correlating one of the gas tracers with either the radio or FIR emission yields basically the same result. There is also a strong resemblance between the $100\text{ }\mu\text{m-H I}$ and CO-H I correlations which is not so easily explained, given the lack of a strong correlation between the $100\text{ }\mu\text{m}$ and CO emission. One possibility is that both the $100\text{ }\mu\text{m}$ and CO emissions reflect the typical sizes of star-forming regions, but in different evolutionary states, whereas the H I emission is dominated by much larger structures.

Within individual sub-regions, cross-correlations of the median filtered 1.4 GHz with the CO and H I are shown in Fig. 9. As expected, for most regions these correlations are much weaker than the cross-correlation of $60\text{ }\mu\text{m}$ with 1.4 GHz radio. Near 30 Doradus (sub-region 8), the integrated H I emission is weakly anti-correlated ($-0.4 < r_w < 0$) with the FIR and radio emission across large and small scales. There is also a weak anti-correlation between the H I and radio emission at $\log(a) \sim 2.7 - 2.8$ for the field containing N11 (sub-region 13); this localised anti-correlation corresponds to the dense, clumpy ring of molecular and atomic gas that surrounds the bright $60\text{ }\mu\text{m}$ and radio source at

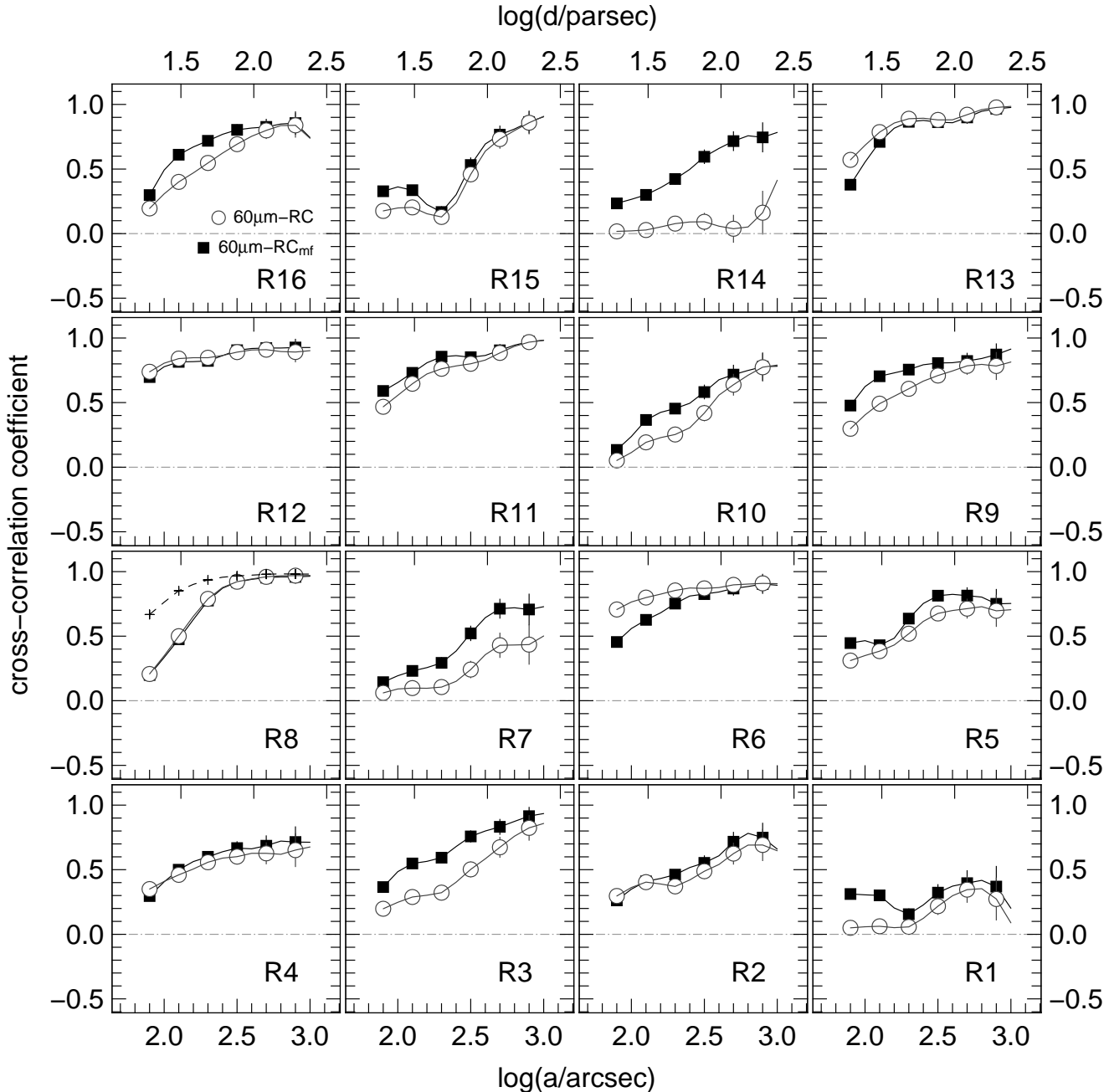


Figure 8. Wavelet cross-correlation spectra in individual sub-regions for the 1.4 GHz radio vs. HIRAS $60\text{ }\mu\text{m}$ emission and median filtered 1.4 GHz radio vs. HIRAS $60\text{ }\mu\text{m}$ emission. For sub-region 8, we also plot the wavelet cross-correlation spectrum for the 1.4 GHz radio vs. HIRES $60\text{ }\mu\text{m}$ emission (crosses). The discrepancy between the cross-correlation results for the HIRAS and HIRES data suggests that resolution effects may be responsible for the poor correlation between the HIRAS $60\text{ }\mu\text{m}$ and the 1.4 GHz radio emission on small scales.

the centre of the N11 star-forming region.

3.5 Decomposition of the Radio Continuum Emission

Previous studies of spiral galaxies have shown that the local FIR-radio correlation is constituted by a correlation between the warm dust and the thermal radio emission, and between the cool dust and the non-thermal radio emission

(Hoernes et al. 1998). In order to investigate whether the good correlation on small spatial scales that we found for some sub-regions is dominated by a correlation between the warm dust and thermal radio emission, we used Parkes maps of the LMC at 1.4 and 4.8 GHz to estimate the thermal fraction of the radio emission across the LMC.

First, the single-dish 1.4 and 4.8 GHz radio maps were smoothed to a common resolution of $15.^{\circ}2$. We then estimated the thermal fraction of the radio emission in

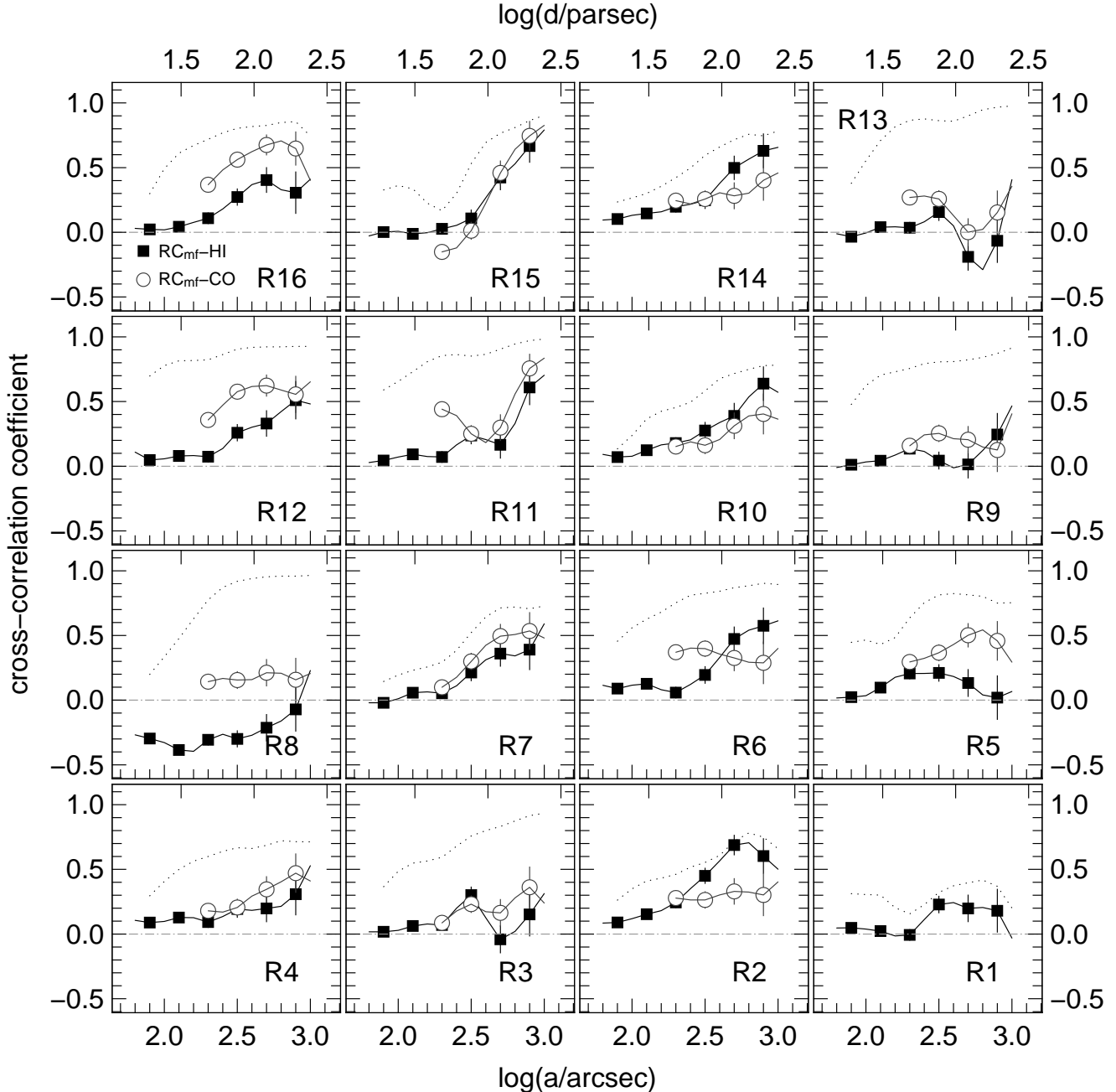


Figure 9. Wavelet cross-correlation spectra in individual sub-regions for the integrated H I vs. 1.4 GHz emission and integrated CO vs. 1.4 GHz emission. The dotted lines show the cross-correlation spectra for the median filtered 1.4 GHz radio vs. 60 μ m emission from Fig. 8. Note that sub-region 1 is poorly covered by our CO map.

each sub-region by applying equation 1 from the paper by Niklas et al. (1997) to the total flux density of each sub-region at 1.4 and 4.8 GHz,

$$\frac{S_{4.8}}{S_{1.4}} = f_{th} \left(\frac{\nu_{4.8}}{\nu_{1.4}} \right)^{-\alpha_{th}} + f_{nth} \left(\frac{\nu_{4.8}}{\nu_{1.4}} \right)^{-\alpha_{nth}}. \quad (13)$$

Here, f_{th} is the thermal fraction of the radio emission at 1.4 GHz, $f_{nth} = 1 - f_{th}$ is the non-thermal fraction, and $S_{1.4}$ and $S_{4.8}$ are the flux densities of each sub-region at 1.4 and 4.8 GHz respectively. For the thermal spectral index, we adopted $\alpha_{th}=0.1$; for the non-thermal spectral index, we used $\alpha_{nth}=0.7$ (Haynes et al. 1991). This simple method of

separation assumes that the emission is optically thin, and that the synchrotron emission can be described by a single power-law over the 1.4 to 4.8 GHz frequency range. We note that our assumption of a constant non-thermal spectral index may introduce a bias in the estimated thermal fraction, since the spectral index is expected to steepen as cosmic rays propagate from their acceleration sites. If these acceleration sites are near star-forming regions, then such regions will have a flatter non-thermal spectral indices than we assume, and thus the thermal fraction will be overestimated. Similarly, the thermal fraction will be underestimated in regions that are far from acceleration

Table 4. Pearson's correlation coefficient, r_p , and wavelet correlation coefficient, r_w , at 4 different spatial scales between image pairs for the whole LMC. The wavelet scales shown are $\log(a) = 2.0, 2.5, 3.0$ and 3.5 , corresponding to spatial scales $d = 25, 80, 245$ and 770 pc. See also Figure 7.

Image pair	r_p	$r_{w,2.0}$	$r_{w,2.5}$	$r_{w,3.0}$	$r_{w,3.5}$
60 μm -RC	0.86	0.27	0.89	0.96	0.98
100 μm -RC	0.85	...	0.79	0.91	0.95
RC-CO	0.20	...	0.13	0.23	0.31
60 μm -CO	0.31	...	0.27	0.34	0.37
RC-H I	0.14	-0.12	-0.11	0.12	0.31
60 μm -H I	0.31	0.06	0.03	0.22	0.33
100 μm -H I	0.48	...	0.16	0.35	0.45
CO-H I	0.37	...	0.12	0.40	0.56

sites. However, the uniform distribution of thermal fractions observed across the sixteen sub-regions (Fig. 10) suggests that this bias is not severe on the scales that we analyse here.

For the radio emission across the whole LMC, we derive a thermal fraction of 0.45. This increases to 0.57 if we restrict our field-of-view to the area of the galaxy that belongs to the 16 sub-regions, suggesting that the diffuse radio emission around the outer edges of the LMC on average has a higher non-thermal fraction than the radio emission within the galaxy. The difference in flux density between the 1.4 GHz emission from the 16 sub-regions and the whole LMC is 62 Jy, so while the radio emission from the galaxy's edges is intrinsically weak, it still makes some contribution to the LMC's total flux density (471 Jy). The results of our decomposition for individual sub-regions are listed in Table 3. The thermal fraction varies from ~ 0.9 for the field containing 30 Doradus, to ~ 0.1 in the south-west of the LMC (sub-region 2). For sub-regions 1 and 14, our decomposition produces an unphysical result, i.e. thermal fractions less than zero. These anomalous values for f_{th} arise because we fix $\alpha_{nth}=0.7$ in our decomposition; both fields are dominated by a bright compact radio point source for which a steeper non-thermal spectral index may be more appropriate. The median thermal fraction for the remaining sub-regions is 0.45, which is higher than the typical value for spiral galaxies (~ 0.1 , Condon 1992), but consistent with radio continuum observations of other dwarf galaxies (Klein et al. 1991; Skillman & Klein 1988). The sub-regions with the highest 1.4 GHz flux density generally have higher thermal fractions. One exception is sub-region 4, the field south of 30 Doradus. Here the thermal fraction is low (0.26), but the 1.4 GHz emission is relatively strong. Previous studies of the polarisation of the radio emission in the LMC have shown that the magnetic field is well-ordered in this region (Klein et al. 1993). Klein et al. (1989) have argued that the higher non-thermal fraction in this part of the LMC arises through a tidal interaction between the LMC and SMC, which drags the magnetic field of the LMC towards the SMC and facilitates the diffusion of relativistic particles into the intergalactic medium.

In the bottom panel of Fig. 10, we plot the spatial scale at which the radio-FIR wavelet cross-correlation falls below

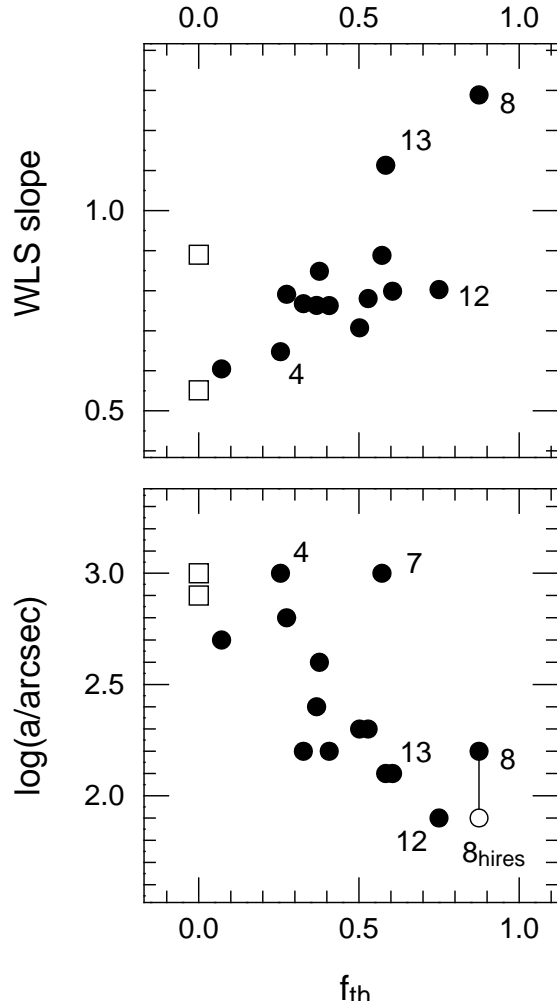


Figure 10. *Top.* The WLS slope of the radio vs. 60 μm relation, plotted against the thermal fraction at 1.4 GHz. Sub-regions where our decomposition method produces thermal fractions less than 0 are plotted as $f_{th} = 0$ with open squares. *Bottom.* The wavelet scale at which the radio-FIR wavelet cross-correlation falls below 0.75, plotted against the thermal fraction of the radio emission at 1.4 GHz. The open circle indicates the result for sub-region 8 using the HIRES 60 μm data.

0.75 against the thermal fraction of each sub-region. For sub-region 8, where the decorrelation at small scales may be partially due to the resolution of the HIRAS FIR data, we also plot the result for the wavelet cross-correlation between the 1.4 GHz and HIRES FIR data (open circle). There is a clear inverse relationship between these two parameters: in sub-regions with a high thermal fraction, the radio-FIR wavelet cross-correlation holds to much smaller scales. We also see a steepening of the WLS fit to the radio-FIR correlation with increasing thermal fraction (top panel of Fig. 10), which is consistent with the increased FIR/radio ratio near star-forming regions discussed in Sections 3.1 and 3.2.

4 DISCUSSION

The primary result of this study is that the local radio-FIR correlation in the LMC is very good: within some regions of the LMC, the 60 μm and 1.4 GHz emission remain strongly correlated down to spatial scales that correspond to the resolution of our data, i.e. ~ 20 pc. On almost all scales that we investigate, the radio-FIR correlation is markedly stronger than the correlation between either the radio or the FIR emission with the gas surface density. However, we also find that the best correlation between the radio and FIR emission occurs in regions where the thermal fraction of the radio emission is high. These regions typically host the brightest emission regions in the LMC, where a steeper than linear correlation is also found. Elsewhere in the LMC, the radio-FIR correlation is flatter, and tends to show a poorer correlation on small spatial scales. In this section, we discuss the results of our analysis in relation to previous studies of the radio-FIR correlation in the LMC. We also consider our results in the context of recent work on the radio-FIR correlation in normal spiral galaxies.

4.1 Comparison with Previous LMC Work

The striking morphological resemblance between the FIR and radio emission has been noted by several previous studies, albeit with lower resolution data than used in this study (e.g. Klein et al. 1989; Xu et al. 1992). In particular, Xu et al. (1992) have studied the correlation between the FIR and 6.3 cm radio continuum emission in the LMC using pixel-by-pixel techniques. The limiting resolution of their data was 4.8 arcmin, allowing them to examine the correlation on spatial scales above 70 pc (for $d_{\text{LMC}} = 50.1$ kpc). Our results are generally in good agreement with the Xu et al. (1992) results. The values that Xu et al. (1992) derive for the correlation coefficient ($r_p=0.84$) between their FIR and 6.3 cm radio map, and their mean FIR/1.4 GHz ratio ($q_{\text{mean}} = 2.40$) are effectively identical to our measurement of these quantities ($r_p=0.86$, and $q_{\text{median}} = 2.45$). Likewise, we find no radial dependence of the FIR/radio ratio.

Through a statistical analysis of 35 H II regions, Xu et al. (1992) have found that the total 6.3 cm radio emission associated with an H II region in the LMC is more centrally concentrated than the total FIR emission, causing the FIR/6.3 cm radio ratio to break down on scales below 70 pc. The authors argued that the central peak in the radio emission – which produces a “dip” in the q -value – should be attributed to thermal radio emission from the ionizing source. At larger radii ($\sim 70 - 200$ pc), they find the FIR/radio ratio to be enhanced, corresponding to the characteristic scale of dust heating around the star-forming region. The Xu et al. (1992) results were based on a statistical analysis of H II regions in their data, but our q -map clearly confirms their description of a “dip-and-ring” morphology for the largest H II regions in the LMC. In Fig. 11, we present a radial analysis of the radio and 60 μm emission associated with N11. Both the radio and the infrared emission show a ring-like morphology: the ring structure is constituted by both bright, well-known star-forming objects and diffuse, filamentary emission at

$r \sim 50-100$ pc from a centre position of $\alpha=4^{\text{h}}56^{\text{m}}43^{\text{s}}$, $\delta=-66^{\circ}29'09''$ (J2000). The 60 μm emission is clearly more extended than the radio emission, however, peaking at larger radii and decaying more gradually towards the background level.

Finally, it is worth noting the discrepancy between our results for the slope of the local FIR-radio correlation (Fig. 3 and Fig. 4) and those of Xu et al. (1992). An unweighted least squares fit to the Xu et al. (1992) data indicated a slope of 0.98 ± 0.02 for the whole LMC, consistent with a linear correlation. However, by determining both the WLS fit and the OLS bisector to our scatterplot of the radio and FIR emission in the whole LMC, and by examining the emission in different sub-regions across the galaxy, we identify a change in the slope of the correlation. This change in slope suggests that there are two distinct physical mechanisms responsible for the correlation. A steeper relation (slope $\sim 1.1 - 1.3$) is found for the high-intensity pixels in the most active star-forming regions, where the thermal fraction of the radio emission is relatively high. A flatter relation (slope $\sim 0.6 - 0.9$) applies more generally to the diffuse radio and FIR emission across the LMC, and in regions with a greater non-thermal contribution to the total radio emission (Fig. 4 and Fig. 10). The most probable reason for the discrepancy between our results and those of Xu et al. (1992) is our ability to sample emission from the LMC more finely, due to the higher angular resolution of our data. Higher resolution permits a better distinction between compact and extended emission than would be possible otherwise.

Our results for the slope of the correlation between the radio and FIR emission are consistent with a cosmic ray diffusion scenario (Bicay & Helou 1990; Murphy et al. 2005), in the sense that while there is an apparent deficit of local radio emission across the LMC, the LMC’s *total* radio flux density is not unusually low. In other words, a flatter than linear slope for the local correlation is not necessarily inconsistent with the linear slope of the FIR-radio correlation for integrated galaxy flux densities, since the integrated flux density measurements used to determine the global correlation can effectively recoup the synchrotron emission from the cosmic ray electrons that have diffused away from their production sites.

4.2 Origin of the global radio-FIR correlation

4.2.1 Star formation models

As discussed in §1, conventional models for the radio-FIR correlation attribute both sources of luminosity to massive star formation. Objections to this explanation are often based on the fact that the FIR is a prompt and relatively local measure of the ionising output of massive stars, while the radio emission results from cosmic ray electron (CRe⁻) energy losses occurring over a much longer timescale and a much larger area. On a globally averaged basis and in a steady-state situation, however, a strong correlation between the radio and FIR emission might still be expected. The sensitivity of synchrotron emissivity to magnetic field strength is not a serious obstacle given that the globally

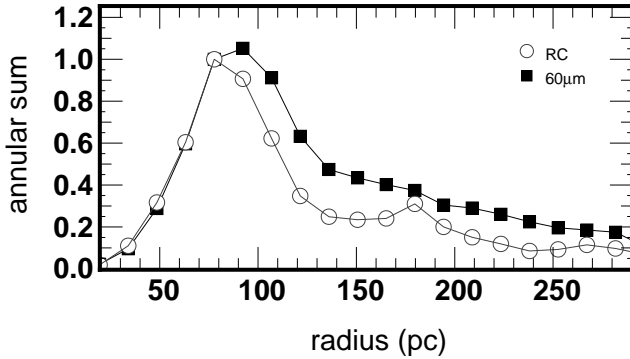


Figure 11. Radial profile of the 60 μm and 1.4 GHz radio emission around N11, centred on $\alpha=4^{\text{h}}56^{\text{m}}43^{\text{s}}$, $\delta=-66^{\circ}29'09''$. The surface brightness in an annulus of radius r , around the central position for the 60 μm emission (filled squares) and the 1.4 GHz radio emission (open circles) is shown. The curves are normalised by their raw value at $r \sim 80$ pc, and the width of each annulus is 15 pc.

integrated emission reflects the total energy emitted by an electron in its radiating lifetime rather than its instantaneous emitted power. On *local* scales, such models predict that the radio emission should appear as a smeared version of the FIR emission, aside from small-scale differences due to temporal fluctuations that violate the steady-state assumption. Support for this prediction comes from the larger radial scale lengths of radio compared to FIR discs (Bicay & Helou 1990; Murphy et al. 2005).

Models in this category include the “calorimeter” model by Völk (1989), in which the production of both UV photons and the relativistic electrons is proportional to the massive star population. The model assumes that in most galaxies the UV photons from massive stars are completely absorbed and reprocessed by interstellar dust, and that relativistic electrons are trapped in the galaxy and lose all their energy through synchrotron or inverse Compton scattering. The energy densities of the magnetic field and the interstellar radiation field are further assumed to be proportional, maintaining a constant ratio of synchrotron to inverse Compton losses. A subsequent, more general version of the calorimeter model by Lisenfeld et al. (1996) allows for finite escape probabilities for relativistic electrons and variable optical depth to UV photons.

With regards to the LMC, three results seem especially relevant. First, the existence of a strong FIR-radio correlation on local scales appears to contradict the calorimeter model, although Fig. 10 implies that this strong correlation is mainly driven by the correlation between *thermal* radio and FIR emission, for which a local correlation is naturally expected. Second, the high thermal fraction of radio emission, coupled with a higher FIR/radio ratio compared to spiral galaxies, suggests that a large fraction of relativistic electrons can escape the LMC, violating the optically thick assumption. In addition, the LMC should be less optically thick to UV photons than massive spiral galaxies because of the lower dust-to-gas ratio (Fitzpatrick 1986) and high porosity implied by the large number of superbubbles and

supershells.

The third argument against the calorimeter model in the LMC is the relatively flat spectral index of $\alpha_{\text{nth}}=0.7$, whereas in the case of efficient cosmic ray trapping one would expect $\alpha_{\text{nth}} \approx 1.1$ (Niklas & Beck 1997). On the other hand, the integrated spectral index is a poor diagnostic of CRe⁻ escape if either the contribution of SNRs to the total radio emission or convective transport of cosmic rays is not negligible (Lisenfeld & Völk 2000). Additional constraints could be provided by examining the variation in spectral index with distance from star-forming regions. Clearly, a more detailed decomposition of the LMC’s radio emission into thermal, diffuse synchrotron, and SNR emission, using multi-frequency high-resolutions data sets, is required to fully address this issue.

4.2.2 Magnetic field – gas density coupling models

An alternative “optically thin model” has been proposed by Helou & Bicay (1993). Once again, the dust-heating UV photons and the cosmic-rays are assumed to have a common origin in massive star formation, but in this case both photons and cosmic rays can escape the galaxy. The radio-FIR correlation is enforced by maintaining equal escape rates for photons and CRe⁻s, i.e. $\tau_0 \propto t_{\text{esc}}/t_{\text{sync}}$, where τ_0 is the UV optical depth, t_{esc} is the CRe⁻ escape time scale, and t_{sync} is the synchrotron loss time scale. In practice, Helou & Bicay (1993) achieve this by coupling the magnetic field B (important for the synchrotron emissivity) to the gas density ρ (important for UV absorption) by the relation $B \propto \rho^{0.5}$, assuming that the typical distance that a CRe⁻ travels before escape (l_{esc}) depends only weakly on the disc scale height (h_0), $l_{\text{esc}} \propto h_0^{0.5}$. Additional assumptions include a nearly constant dust-to-gas ratio, in agreement with observations (e.g., Xu & Helou 1996), and a proportionality between synchrotron and inverse Compton losses, as in the calorimeter model. The physical basis for the B - ρ coupling could be amplification of MHD turbulence until energy equipartition is reached (Groves et al. 2003).

Other models in this class differ slightly in their prescription for cosmic-ray confinement (and hence number density). Helou & Bicay (1993) assume a confinement process such that $l_{\text{esc}}h_0^{-0.5}$ is constant, Niklas & Beck (1997) assume equipartition between the CRe⁻ density (n_{CR}) and magnetic field, $n_{\text{CR}} \propto B^2 \propto \rho$, and Hoernes et al. (1998) assume a nearly constant CRe⁻ density, as do Murgia et al. (2005). In spite of these differences, which may simply reflect our poor understanding of how cosmic rays are distributed, the basic condition of $B \propto \rho^{0.5}$ is common to all of these models, and is motivated by the sensitive dependence of synchrotron emission on the magnetic field strength, bearing in mind the large range of magnetic field strengths observed in galaxies obeying the correlation (Condon et al. 1991). These models have the advantage of naturally producing a *local* radio-FIR correlation, breaking down only on scales $\sim l_{\text{esc}}$ due to cosmic ray diffusion. The fundamental B - ρ coupling, moreover, could be valid down to the scales of typical gas clouds (~ 100 pc). Most significantly, the coupling can even produce a radio-FIR

correlation in cases where the FIR is dominated by cool dust heated by older stellar populations, although the correlation would not necessarily be linear (Hoernes et al. 1998).

Do our LMC results support the idea of a coupling between magnetic field and gas density? Although there is a general morphological correspondence between the large-scale features of the neutral gas and the radio and FIR maps, the H_I and CO emission are poorly correlated with the radio emission on scales below ~ 1 kpc (Figs. 7 and 9). Even in regions with significant non-thermal radio fractions, the radio-FIR correlation cannot be simply derived from a correlation between the H_I (which dominates the total gas content) and the radio continuum. Note however that the synchrotron emission depends on the number density of relativistic electrons as well as the magnetic field strength; Helou & Bicay (1993) constrain n_{CR} by assuming that $l_{\text{esc}} \propto h_0^{0.5}$, but provide only qualitative arguments to justify this assumption. If the escape length for cosmic rays in the LMC is significantly shorter than a nominal value of ~ 2 kpc – for example because of a high porosity of the ISM – then the galaxy cannot effectively extract energy from the cosmic rays it generates, even if B attains values typical of spiral galaxies. Thus, it is still possible that B - ρ coupling holds in the LMC, but that the CR electrons are not able to fully explore the dense gas distribution. Direct measurements of the local magnetic field strength throughout the LMC, e.g. through Faraday rotation (Gaensler et al. 2005), will be required to rigorously test the B - ρ coupling model.

We can, however, address the suggestion by Niklas & Beck (1997) that the FIR emission is coupled to the gas density via the Kennicutt-Schmidt law, $\rho_{\text{SFR}} \propto (\rho_{\text{gas}})^{1.4}$, and that this combined with B - ρ_{gas} coupling leads to a tight radio-FIR correlation. Our wavelet cross-correlation analysis shows that the FIR emission is much more poorly correlated with the gas column density than with the radio emission, even in sub-regions where the thermal radio fraction is relatively small. Thus, it appears unlikely that the Kennicutt-Schmidt law can serve as a basis for understanding the radio-FIR correlation.

4.2.3 Connection of FIR-radio correlation to molecular gas

Recently, Murgia et al. (2005) have demonstrated that the CO-radio correlation within spiral galaxies is as strong as the FIR-radio correlation down to scales of ~ 100 pc. They explain both by arguing that the gas density and magnetic field strength are linked via equipartition between turbulent and magnetic pressure in a hydrostatic disc. However, our results indicate a relatively poor correlation between CO and 1.4 GHz radio emission within the LMC (Fig. 7). We identify several possible reasons for the difference between our results and those of Murgia et al. (2005). First, the thermal radio fraction f_{th} is much higher for the LMC than in spiral galaxies, so one expects the CO-radio correlation on small scales to behave more like the CO-60 μm correlation, breaking down near H II regions due to the photodestruction of molecular clouds. Second,

the fraction of neutral gas mass in molecular form, f_{mol} , is much smaller in the LMC, ~ 0.05 assuming a Galactic CO-to-H₂ conversion factor, compared to $\gtrsim 0.5$ in the central regions of massive galaxies studied by Murgia et al. (2005) (cf. Wong & Blitz 2002). Since CO cannot survive without self-shielding, this results in a much lower volume filling factor for CO emission, and thus no CO counterpart to the extended non-thermal radio emission. Finally, the combination of strong external pressures exerted on the LMC due to its interaction with the Milky Way halo and variable internal pressures due to the expansion of bubbles and supershells suggests that simple estimates of the hydrostatic pressure will not predict the distribution of CO clouds. Indeed, observations of the LMC 4 supershell by Yamaguchi et al. (2001) provide evidence for the formation of molecular clouds in the swept-up H_I surrounding the supershell.

5 CONCLUSIONS

We have examined the correlation between the 1.4 GHz radio continuum and 60 μm emission in the LMC, using pixel-by-pixel techniques and a wavelet cross-correlation method. The correlations between the radio continuum, FIR emission and the integrated ¹²CO and H_I emission have also been studied, in order to assess the relevance of gas density for the local radio-FIR correlation. The high angular resolution datasets that are available for the LMC allow us to probe the radio-FIR correlation on spatial scales above ~ 20 pc, and to identify variations of the FIR/radio ratio for different interstellar environments.

The main results of our study are:

1. Pearson's correlation coefficient shows that the 1.4 GHz and 60/100 μm are positively correlated across the LMC. The correlation coefficient for 1.4 GHz and 60 μm emission in the whole LMC is ~ 0.86 , indicating a strong correlation. The correlation improves in regions where there are clear signs of star-forming activity, e.g. near 30 Doradus. The correlation between the radio and FIR emission is significantly stronger than correlations between these wavebands and cold gas tracers.
2. Pixel-by-pixel scatterplots indicate that locally there are two independent correlations between the radio and FIR emission, both of which are non-linear. A steeper than linear correlation (slope $\sim 1.1 - 1.3$) is found for the high-intensity pixels in the most active star-forming regions, where the thermal fraction of the radio emission is relatively high. A flatter correlation (slope $\sim 0.6 - 0.9$) applies more generally to the diffuse radio and FIR emission across the LMC, and in regions with a greater non-thermal contribution to the total radio emission.
3. Both the integrated FIR/radio ratio ($q = 2.55$) and the median FIR/radio ratio across the LMC ($q_{\text{median}} = 2.45$) are higher than the mean FIR/radio ratio of the Yun et al. (2001) galaxy sample ($q_{\text{mean}} = 2.34$), suggesting that the radio emission in the LMC is slightly underluminous, or

that there is a slight excess of FIR emission. In contrast to nearby spiral galaxies, the brightest structures in the FIR/radio ratio map of the LMC do not correspond to the brightest structures in the input FIR and radio maps.

4. A simple decomposition of the 1.4 GHz radio emission indicates that the thermal fraction of the LMC is higher than for normal disc galaxies (~ 0.1 , Condon 1992). For an assumed non-thermal spectral index of $\alpha_{nth}=0.7$, the thermal fraction for the whole the LMC is 0.45, varying between 0 and 0.9 for individual sub-regions. The high FIR/radio ratio and high thermal fraction of the LMC's radio emission suggests that a large proportion of CRe⁻s may be escaping from the LMC with low synchrotron losses.

5. Wavelet cross-correlation spectra show that the correlation between the 1.4 GHz radio continuum and 60 μm emission is very good across the LMC, even on scales corresponding to a few tens of parsecs. For the whole LMC, the correlation between the radio and 60 μm emission on all scales is significantly better than the correlation of the H I or CO with either the radio or FIR emission. We argue, however, that the excellent correlation between the radio and FIR emission for the LMC as a whole is driven by the 30 Doradus region. For individual sub-regions within the LMC, there is an inverse relationship between the scale on which the correlation breaks down and the thermal fraction of the radio emission: regions that show a strong correlation to small spatial scales are also the regions where the thermal fraction of the radio emission is high. In regions where the thermal fraction is less than 0.5, the wavelet cross-correlation between radio and 60 μm emission breaks down across a range of scales between 50 and 250 pc.

While models for the radio-FIR correlation typically address the emission and coupling mechanisms in normal spiral galaxies, the LMC remains an interesting testbed because of the wide range of angular scales that can be probed. The presence of a strong local radio-FIR correlation that is dominated by high-brightness thermal emission, combined with evidence for a diffuse non-thermal radio component that contributes to the LMC's total radio flux density, underscores that different phenomena can be responsible for brightness as opposed to integrated flux density. This distinction should be kept in mind in future studies of more massive galaxies.

We would like to thank the referee, John Dickel, for his careful reading and astute comments that improved the final version of this paper significantly. We also thank Jason Surace, Michael Braun, Sunguen Kim, John Dickel, Uli Klein, and Marc-Antoine Miville-Deschénes for access to the datasets that were used in this study. Rainer Beck and Eric Murphy contacted us about this work prior to publication, and our understanding has benefitted from their insight and expertise. AH enjoyed illuminating discussions with Vince McIntyre, Steve Ord, Juergen Ott, Erik Muller, Jean-Phillipe Bernard, Roberta Paladini and Michael Dahlem, and would like to thank Christophe Pichon and Eric Thiébaut for developing many invaluable YORICK routines that were used in this work.

REFERENCES

Alves D. R., 2004, New Astronomy Review, 48, 659
 Appleton P. N., et al., 2004, ApJS, 154, 147
 Bicay M. D., Helou G., 1990, ApJ, 362, 59
 Bontekoe T. R., Koper E., Kester D. J. M., 1994, A&A, 284, 1037
 Boulanger F., Perault M., 1988, ApJ, 330, 964
 Braun M., Assendorp R., Bontekoe D. J. M., Kester T. R., Richter G., 1998, in The Magellanic Clouds and Other Dwarf Galaxies, Richter T., Braun J. M., eds., Shaker Verlag, Aachen, pp. 121–124
 Cohen M., Green A. J., 2001, MNRAS, 325, 531
 Condon J. J., 1992, ARA&A, 30, 575
 Condon J. J., Huang Z.-P., Yin Q. F., Thuan T. X., 1991, ApJ, 378, 65
 Elmegreen B. G., Kim S., Staveley-Smith L., 2001, ApJ, 548, 749
 Feigelson E. D., Babu G. J., 1992, ApJ, 397, 55
 Filipovic M. D., Haynes R. F., White G. L., Jones P. A., Klein U., Wielebinski R., 1995, A&AS, 111, 311
 Fitzpatrick E. L., 1986, AJ, 92, 1068
 Frick P., Beck R., Berkhuijsen E. M., Patrickeyev I., 2001, MNRAS, 327, 1145
 Fukui Y., Mizuno N., Yamaguchi R., Mizuno A., Onishi T., 2001, PASJ, 53, L41
 Fukui Y., et al., 1999, PASJ, 51, 745
 Gaensler B. M., Havercorn M., Staveley-Smith L., Dickey J. M., McClure-Griffiths N. M., Dickel J. R., Wolleben M., 2005, Science, 307, 1610
 Groves B. A., Cho J., Dopita M., Lazarian A., 2003, PASA, 20, 252
 Haslam C. G. T., Osborne J. L., 1987, Nature, 327, 211
 Haynes R. F., Murray J. D., Klein U., Wielebinski R., 1986, A&A, 159, 22
 Haynes R. F., et al., 1991, A&A, 252, 475
 Helou G., Bicay M. D., 1993, ApJ, 415, 93
 Helou G., Soifer B. T., Rowan-Robinson M., 1985, ApJ, 298, L7
 Hippelein H., Haas M., Tuffs R. J., Lemke D., Stickel M., Klaas U., Völk H. J., 2003, A&A, 407, 137
 Hoernes P., Berkhuijsen E. M., Xu C., 1998, A&A, 334, 57
 Kim S., Dopita M. A., Staveley-Smith L., Bessell M. S., 1999, AJ, 118, 2797
 Kim S., Staveley-Smith L., Dopita M. A., Freeman K. C., Sault R. J., Kesteven M. J., McConnell D., 1998, ApJ, 503, 674
 Kim S., Staveley-Smith L., Dopita M. A., Sault R. J., Freeman K. C., Lee Y., Chu Y., 2003, ApJS, 148, 473
 Klein U., Haynes R. F., Wielebinski R., Meinert D., 1993, A&A, 271, 402
 Klein U., Weiland H., Brinks E., 1991, A&A, 246, 323
 Klein U., Wielebinski R., Haynes R. F., Malin D. F., 1989, A&A, 211, 280
 Lisenfeld U., Völk H. J., 2000, A&A, 354, 423
 Lisenfeld U., Völk H. J., Xu C., 1996, A&A, 306, 677
 Marx M., Dickey J. M., Mebold U., 1997, A&AS, 126, 325
 Mathewson D. S., Ford V. L., Tuohy I. R., Mills B. Y., Turtle A. J., Helfand D. J., 1985, ApJS, 58, 197
 Meaburn J., 1980, MNRAS, 192, 365
 Miville-Deschénes M.-A., Lagache G., 2005, ApJS, 157, 302
 Mizuno N., et al., 2001, PASJ, 53, 971

Munro D., 1995, Computers in Physics, 9, 609

Murgia M., Helfer T. T., Ekers R., Blitz L., Moscadelli L., Wong T., Paladino R., 2005, A&A, 437, 389

Murphy E. J., et al., 2005, astroph/0510227, 000, 000

Niklas S., Beck R., 1997, A&A, 320, 54

Niklas S., Klein U., Wielebinski R., 1997, A&A, 322, 19

Press W. H., Teukolsky S. A., Vetterling W. T., Flannery B. P., 1992, Numerical recipes in FORTRAN, 2nd edn. Cambridge U. Press, Cambridge

Sault R. J., Teuben P. J., Wright M. C. H., 1995, in ASP Conf. Ser. 77: Astronomical Data Analysis Software and Systems IV, pp. 433–+

Skillman E. D., Klein U., 1988, A&A, 199, 61

van der Hulst J. M., Terlouw J. P., Begeman K. G., Zwitser W., Roelfsema P. R., 1992, in ASP Conf. Ser. 25: Astronomical Data Analysis Software and Systems I, pp. 131–+

Völk H. J., 1989, A&A, 218, 67

Walterbos R. A. M., Schwering P. B. W., 1987, A&A, 180, 27

Whiteoak J. B. Z., Green A. J., 1996, A&AS, 118, 329

Wong T., Blitz L., 2002, ApJ, 569, 157

Xu C., Helou G., 1996, ApJ, 456, 163

Xu C., Klein U., Meinert D., Wielebinski R., Haynes R. F., 1992, A&A, 257, 47

Yamaguchi R., Mizuno N., Onishi T., Mizuno A., Fukui Y., 2001, PASJ, 53, 959

Yun M. S., Reddy N. A., Condon J. J., 2001, ApJ, 554, 803